Master's Thesis

Multilayered Ferroelectric Hybrid Materials for Enhanced Triboelectric Nanogenerators

Yoojeong Park

Department of Chemical Engineering

Graduate School of UNIST

2019

Multilayered Ferroelectric Hybrid Materials for Enhanced Triboelectric Nanogenerators

Yoojeong Park

Department of Chemical Engineering

Graduate School of UNIST

2019

Multilayered Ferroelectric Hybrid Materials for Enhanced Triboelectric Nanogenerators

Yoojeong Park

Department of Chemical Engineering

Graduate School of UNIST

Multilayered Ferroelectric Hybrid Materials for Enhanced Triboelectric Nanogenerators

A thesis/dissertation
submitted to the Graduate School of UNIST
in partial fulfillment of the
requirements for the degree of
Master of Science

Yoojeong Park

07. 09. 2019
Approved by

Advisor
Hyunhyub Ko

Multilayered Ferroelectric Hybrid Materials for Enhanced Triboelectric Nanogenerators

Yoojeong Park

This certifies that the thesis/dissertation of Yoojeong Park is approved.

07. 09. 2019

signature

Advisor: Hyunhyub Ko

signature

Jiseok Lee

signature

Seok Ju Kang

Abstract

The flexible triboelectric nanogenerators (TENGs) enabling high power generation have been a great attention for applications in self-powered sensors and wearable devices. Conventionally, many researches have employed inorganic ferroelectric materials with high dielectric constant into elastomers or ferroelectric polymer matrix for high-performance TENGs. However, randomly dispersed inorganic materials in composites prevent the effective stress-transfer for the stress-induced polarization of ferroelectric composites. Here, we introduce novel high performance TENGs based on multilayered ferroelectric organic/inorganic materials. The multilayers consisting of PVDF-TrFE layers and aligned BTO nanoparticle (NP) interlayers can increase the effective stress-induced polarization, which improves the surface potential for the enhanced triboelectric output performances. This surface potential is additionally enhanced by the electrical poling process. As a result, the output current density of multilayered TENGs with aligned BTO NPs is increased ~ 47% compared to the single composite TENGs with randomly dispersed BTO NPs. Furthermore, the multilayered TENGs exhibit tunable frequency sensing capability by controlling the number of multilayers, providing a possible application in acoustic sensors with frequency selectivity. Our findings on multilayered TENGs would offer a great potential for self-powered sensors and wearable electronics.

KEYWORDS: triboelectric nanogenerator, multilayered film, surface charge density, surface potential, polarization, ferroelectric material

Contents

List of figures

of the PVDF-TrFE film and the PVDF-TrFE/BTO film.

Figure 3.6. Schematic of BTO coated on the PVDF-TrFE with different concentrations of BTO/EtOH solution and output current and voltage of the single PVDF-TrFE film with BTO interlayer.

Figure 3.7. (a) Schematics of working principle in the polarized PVDF-TrFE/BTO film. (b) Working mechanism of the TENG with the polarized ferroelectric materials.

Figure 3.8. Schematics of (a) the multilayered PVDF-TrFE and (b) the multilayered PVDF-TrFE/BTO. Output voltage and current of (c and e) the multilayered PVDF-TrFE and (d and f) the multilayered PVDF-TrFE/BTO film at different number of layers, ranging from 1 to 7.

Figure 3.9. (a) Schematics of the four-layered PVDF-TrFE/BTO film based TENGs. Schematics and output current of the four-layerd PVDF-TrFE/BTO film with (b) non-polarization state (c) positive polarization state (d) negative polarization state.

Figure 3.10. (a) Schematics of the four different types of samples with the same thickness: single PVDF-TrFE, multilayered PVDF-TrFE, single PVDF-TrFE/BTO, multilayered PVDF-TrFE/BTO. Comparison of (b) the output current and (c) voltage of the four different types of samples (d) Thermogravimetric analysis (TGA) result of the four-layerd PVDF-TrFE/BTO film.

Figure 3.11. (a) Schematics of the four different types of samples with the same thickness: single PVDF-TrFE, multilayered PVDF-TrFE, single PVDF-TrFE/BTO, multilayered PVDF-TrFE/BTO. (b) Piezoelectric current and voltage of the four different types of samples.

Figure 3.12. Schematics and output current of the TENGs (a) in the forward connection (b) in the reverse connection.

Figure 3.13. (a) Output current and (b) voltage of the non-poled and poled four-layered PVDF-TrFE/BTO film. (c) Output voltage and (d) current of the TENGs depending on the applied pushing force up to 98 kPa.

Figure 3.14. (a) Output voltage and current at different loading resistance, ranging from 1 kΩ to 750 MΩ. (b) Optimized maximum output power density at 100 MΩ. (c) Rectified voltage of the

four-layerd PVDF-TrFE/BTO film and photographs showing the ability of TENGs to drive LEDs

Figure 3.15. (a) Schematic image and (b) photograph of acoustic sensor consists of the multilayered film and ITO/PET film. (c) Schematics of oscillating multilayered film with acoustic energy.

Figure 3.16. Characterization of the frequency selective acoustic sensor. (a) Electrical properties of the acoustic sensor based on multilayered triboelectric nanogenerator. The inset displays the schematics of multilayered film having different oscillating behavior according to the thickness of film. (b) Fast Fourier transform (FFT) of the frequency selective acoustic sensor.

1. Introduction

1.1 Triboelectric energy harvesting devices

Energy harvesting technologies that can scavenge abundant energies from solar power,[1, 2] thermal energy,[3, 4] and wind energy[5-7] have attracted as promising power sources for various applications (**Figure 1a**).[8] Above all, the scavenging of mechanical energies by piezoelectric,[9] electromagnetic,[10] and electrostatic properties[11] have received a great attention for new energy generation.[12] Although the mechanically-induced energies show a less power density than solar energy, there are their beneficial advantages of sustainability independent from environmental conditions, universality, and flexible and wearable characteristics. Based on these characteristics, energy harvesting devices from mechanical energies have been applied to low-power consumption electronics, self-powered sensors, wearable devices, wireless transmitters, and body implantable devices **(Figure 1b).**[13-21]

Among the various energy harvesting systems, triboelectric nanogenerators (TENGs) have been regarded as a promising candidate for next-generation energy harvesting device due to their significant merits of high power density, low-cost, and easy fabrication process.[22, 23] The TENG devices can convert mechanical energy to electrical energy by coupling effect between triboelectrification and electrostatic induction. In specific, when two materials with different tribo-polarities come in contact with each other, charge transfer at the contacting surface forms the electrical potential (triboelectrification), and subsequently the electron is driven to flow through externally connected circuit for balancing the electrical potential (electrostatic induction). This simple triboelectric mechanism enables to harvest various mechanical energies from wasted sources in our daily life such as human motions, transportation, and wasted environmental changes. Furthermore, the electrical outputs are proportionally increased by mechanical intensity, which can be available for self-powered mechanical sensors.

For the development of TENG technologies, recently various advanced TENGs have been reported by introducing structural and material approaches.[20] The structural approach is to design various multi-dimensional architectures, which provide a large surface area under the application of mechanical stress, thus resulting in enhanced triboelectricity.[15] In addition, the material approach with chemically functionalized surface and modulation of permittivity enhances the triboelectric performances due to the large difference in surface polarity between the contacting two materials.[24] Furthermore, the introduction of post processing methods such as electrical poling and hybridization with different-typed energy harvesting device also become a beneficial tool for improving triboelectric power generation.[25] Based on these approaches, recent TENG

devices have provided new opportunities as an alternative energy source for future applications such as wearable and implantable electronics, robotics, and smart devices.

1.2. Working mechanism of triboelectric nanogenerators

Recent TENGs have been demonstrated by three basic operation modes: vertical contact-separation mode, single-electrode mode, and parallel sliding mode. These TENG devices are driven by conjugation with two effects of triboelectrification and electrostatic induction. For detailed working mechanism, the vertical contact-separation mode is illustrated in **Figure 1.2**.[23, 26] The vertical-separation mode is the most common model, which consists of two neighboring thin organic/inorganic films with different surface polarities. For example, a Kapton film and a PMMA film are used as triboelectric active layers, respectively. Two different materials are face-to-face each other and the electrodes are deposited on the two films. In the original state, there is no charge transfer (I). When two materials are in contact under external forces, the Kapton and PMMA films are gaining and losing charges through friction, respectively. Thus, triboelectric opposite charges are generated between the two surfaces of materials due to the triboelectric effect. The surface of PMMA is positively charged and the surface of Kapton is negatively charged after contact (II). Once the external force is released, a potential difference appears between the two materials. Due to the electrostatic induction effect, free electron in the bottom electrode will flow to the top electrode though the external circuit to compensate this potential difference, creating a current pulse (III). This flow continues until neutralized (V). When two materials are closed again, the triboelectric potential difference disappears and the free electron flow back into the circuit, creating an opposite current pulse (VI). The current generated from triboelectric nanogenerator by friction between the two materials can be defined as follows,[15]

$$\mathrm{I} = \mathrm{C}\frac{\partial V}{\partial t} + V\frac{\partial C}{\partial t} \qquad \textbf{(1)}$$

where C is the capacitance, V is the voltage across the two electrodes, and I is the current across an external load.

There are two different types of factors to determine the output current generated from triboelectric nanogenerators. One is the potential difference established between the two electrodes. Due to the electrostatic induction effect, electrons flow between the two electrodes through external circuit to equilibrate the potential difference. The other one is the variation in capacitance. As the distance between the two electrodes is varied, the capacitance of the system changes under mechanical deformation of the triboelectric friction layer.

1.3. Strategies for enhanced triboelectric performances

Recently, there has been great achievements in enhancing the performances of triboelectric nanogenerators, relying on the rational design of materials and structural modifications. The material design is closely related to the surface treatment of contacting materials for tuning of the difference in surface polarity between contacting materials. In addition, structural modification includes the introduction of various micro/nanostructures and macroscopic control of device architectures.

1.3.1. Surface functionalization

Surface functionalization by molecular engineering can be an effective method for enhancing triboelectric property.[27] Chemically modified surface charge by self-assembly of monolayers using end-fluorine terminated group, thiol with different head-group, and atomic-level halogens and amines influences on surface potential and surface charge density, directly affecting the triboelectric output. Therefore, many researchers have investigated surface functionalization in order to increase the potential difference between two contacting triboelectric materials. For instance, the negative triboelectric materials which have many fluoro (-F) atoms on its surface have high electron affinity.

As shown in **Figure 1.3a**, the surface of PET films were functionalized by poly-L-lysine solution and trichloro (1H,1H,2H,2H,-perfluorooctyl) silane (FOTS) vapor, respectively.[28] The surface of PET functionalized with amino ($-NH_3^+$) end group is positively charged, while the PET surface with fluorine (F) atoms is negatively charged. The two PET films with positive and negative charges have a significant difference in polarity. The resulting triboelectric nanogenerator can achieve the maximum open-circuit voltage of ~330 V, which is 4 times higher than non-functionalized PET. Furthermore, **Figure 1.3b** introduces the surface functionalized TENGs with various functional groups of self-assembled mono-layers (SAMs) to increase the output performance.[24] The device that has FOTS modified surfaces exhibits the maximum output voltage and current of 105 V and 27 μA, respectively. The device composed of 1 H,1H,2H,2H-perfluorooctyltrichlorosilane (FOTS) modified film and Al shows more than 4 times higher output performance than unmodified PDMS/Al device.

1.3.2. Surface morphology

In addition to molecular design of surface, modification of surface morphology can be another strategy for improving the output performance of triboelectric nanogenerator. Especially, instead of a flat surface, introducing patterned surfaces such as pyramid-, cube- or line-shaped micro- and nano-patterns significantly increase the contact area between the triboelectric active layers. As

shown in **Figure 1.4a**, the TENGs with pyramid or cube microstructures exhibit 5-6 times higher output performance than those with flat films.[15] In addition, nanopatterned surface morphologies such as nanodots, nanogrates, and nanomeshes can also enhance the triboelectric output, which is caused by the large surface area of nanostructured patterns (**Figure 1.4b).**[29]

1.3.3. Device architecture

Various device architecture of bulk triboelectric systems have been proposed to enhance energy harvesting performance of TENGs.[30] For examples, macroscopically designed architectures such as multi-stacking,[31-33] rotating,[34-36] and textile[37-41] have been applied to increase the amount of charge generation due to the large contact area and high variation in the distance between the triboelectric materials. The multi-stacked structure of unit cells connected in parallel can enhance the output performance of TENGs through the simple fabrication process (**Figure 1.5a and 1.5b**). **Figure 1.5a** shows the multilayer-stacked three layers on the zigzag-shape substrate.[42] Due to expanded contact area, these triboelectric sensors generate open-circuit voltage and short-circuit current up to 220 V and 600 μA, respectively. In addition, the paper-based rhombic-shaped device is presented in **Figure 1.5b.**[43] It was found that the TENGs with assembled units have higher output charges than one unit in charging curves. Due to its ultralight property, the device can be used for portable self-powered electronics. **Figure 1.5c and 1.5d** presents rotation-induced TENGs with the sliding working mode unlike the vertical contact mode. **Figure 1.5c** introduces the traditional disk-shape TENGs for harvesting rotational mechanical energy.[44] The output current of the device is affected by rotating speed and segmentation number. Recently, low friction triboelectric-electromagnetic NGs are introduced **(Figure 1.5d)**.[45] Compared to conventional TENGs based on large friction force, this freestanding mode TENG provides a low friction force, resulting in current driving from the low input energy. The textile based TENGs have great attention due to their high flexible and wearable properties. **Figure 1.5e** shows the woven structured TENGs using commercial nylon, polyester, and silver fiber fabric.[16] Because of its textile characteristic, the TENGs have wearable, washable, breathable properties. **Figure 1.5f** introduces electronic textile based TENGs. Because the device is composed of a flexible textile substrate, it can demonstrate the high stretchability/flexibility, washability and air permeability.[46]

1.4. Effect of electrical polarization in the ferroelectric materials

To further enhance the triboelectric property, there has been recent attempts to use ferroelectric polarization for increasing surface charge density.[47] The surface charge density can be changed by charge transfer which is proportional to the surface potential difference between two contacting materials. Therefore, controlling the surface potential of ferroelectric materials can be an effective way to improve the triboelectric property, which is primarily proceeded through the electrical polarization process.[48]

1.4.1. Control of ferroelectric polarization

As shown in **Figure 1.6,** controllable triboelectric properties of poly(vinylidenefluoride-co-trifluoroethylene) (PVDF-TrFE) depending on its polarization direction and intensity are reported. When electric field is applied on the ferroelectric PVDF-TrFE, the dipoles in PVDF-TrFE are aligned in the same direction with electric field.[49, 50] These aligned dipoles form a surface potential in ferroelectric polymer. It is determined whether the surface potential is negative or positive depending on the direction of polarization.[51] The PFM and KPFM image (**Figure 1.6a-i,ii)** shows the negatively and positively polarized PVDF-TrFE surface, creating the negative and positive surface potential, respectively.[52]

Generally, human skin is placed at the positive side in the triboelectric series. **(Figure 1.6b)** Thus, the human skin is positively charged after contact with non-polarized PVDF-TrFE film. However, when the negatively polarized PVDF-TrFE and human skin are in contact, the human skin obtains charges from poled PVDF-TrFE and becomes negatively charged (**Figure 1.6a).** This behavior is because the negatively polarized PVDF-TrFE has higher positive triboelectric properties than the skin in the triboelectric series and acts as positive triboelectric material. This phenomenon demonstrates that the polarization direction of ferroelectric material can affect the triboelectric property which determines the tendency to lose or gain electrons.

Figure 1.6b shows the output voltage of TENGs generated by friction between the skin and PVDF-TrFE film with different polarization direction and intensity. The non-poled PVDF-TrFE film exhibits low output performance. Positively polarized PVDF-TrFE has a higher output voltage than non-polarized PVDF-TrFE under electric fields ranging from 25 to 100 MV/m (left side). This result is because PVDF-TrFE which has positive surface potential is located in a more negative side in triboelectric series than non-polarized PVDF-TrFE. Therefore, high surface potential difference between positively polarized PVDF-TrFE and skin causes enhanced output performance. Reversely, the negatively polarized PVDF-TrFE shows the opposite behavior of triboelectric signal under electric field of 50 and 100 MV/m (right side). The opposite signal

indicates that the human skin gains electrons from the poled PVDF-TrFE. In addition, the output performance can be improved as the polarization intensity is increased from 25 to 100 MV/m.

1.4.2. Enhancement of surface charge density by ferroelectric polarization

The output performance of triboelectric nanogenerators are determined by the surface charge density on triboelectric friction layers during the contact-separation process. Poled PVDF-TrFE has an efficient charge transfer capability, resulting in a large surface charge density during friction. It is well known that the larger the surface potential difference between the two materials, the more charges are transferred. The surface potential can be increased through the ferroelectric polarization. As shown in **Figure 1.7a-i**, the COMSOL multiphysics simulation results show a greater surface potential difference between poled PVDF-TrFE and skin than non-poled PVDF-TrFE.[25] In addition, the energy band gap results demonstrate the poled PVDF-TrFE engages a lot of charges from Al, which is because the band gap shifts by positively polarized PVDF-TrFE (**Figure 1.7a-ii).** In **Figure 1.7a-iii**, the output voltage and current of TENGs are increased after poling the PVDF-TrFE. Additionally, $BaTiO_3$ with the high dielectric constant can improve the output performance by increasing capacitance in the composite.

It is demonstrated that the output performance and triboelectric properties of TENGs are affected by the polarization direction as illustrated in **Figure 1.7b**.[48] The non-polarized and positively polarized PVDF-TrFE have negative triboelectric properties compared to Al, causing the same signal shapes (positive signal is first) of output voltages. However, the negatively polarized PVDF-TrFE has positive properties than Al, resulting in the opposite peak shapes (negative signal is first) of outputs. In addition, both poled PVDF-TrFE have a high surface potential than non-poled PVDF-TrFE, which can enable to increase the output performance of TENGs.

1.5. Triboelectric nanogenerators based on ceramic/polymer composites

Using composite materials composed of polymer and ceramic nanoparticles is an well-known approach for enhancing the output performance of TENGs.[53, 54] Ceramic material which has a high dielectric constant and ferroelectric property are useful to achieve high output performance of TENGs. However, high stiffness and brittleness properties of ceramic materials have limitations for wearable and flexible device applications. Therefore, the composite type TENGs composed of a randomly dispersed ceramic powder and flexible polymer matrix show good mechanical flexibility and ferroelectric/dielectric properties. In addition, many researches introduce that the TENGs with ceramic material can increase the output performance through their 1) high permittivity and 2) the polarization effect.

1.5.1. High dielectric inorganic ferroelectric materials

Inorganic ferroelectric materials such as PZT,[55] ZnO,[56] $NaNbO_3$,[57] PMN-PT,[58] $BaTiO_3$ [59, 60] have been widely used for high performance energy harvesting devices due to high dielectric constant. In addition, the high permittivity of inorganic materials increases the ability of attracting charges, leading to the enhancement of the triboelectric charge density. Due to limited flexibility and high brittleness, inorganic ferroelectric materials have been mainly used by mixing with elastomeric polymers. As shown in **Figure 1.8a**, when the $BaTiO_3$ film and PTFE film is contacted, the potential difference between the two surfaces cause a polarization of ferroelectric $BaTiO_3$.[61] As a result, polarized $BaTiO_3$ with high permittivity can help PTFE acquire more charges. In addition, the $NaNbO_3$/PDMS composite TENGs with high permittivity increases the output performance (**Figure 1.8b**).[57] The concentration of cubic $NaNbO_3$ NPs affects the capacitance of the system, which is an important factor to determine the output performance of composite. **Figure 1.8c** shows the composite consists of PVDF-TrFE and high dielectric material, $BaTiO_3$.[25] Since the high permittivity of $BaTiO_3$ can increase the capacitance of the TENGs, the output performance can improve the amount of triboelectric charges generated from TENGs, which can be defined as follows,[25]

$$Q = CV \qquad \textbf{(2)}$$

Q : surface charge

C : capacitance of the system

V : voltage generated from triboelectric effect

From this equation, it is known that the surface charge is increased with increasing the capacitance

of composite by including high dielectric ceramic material inside the polymer matrix.

1.5.2. Polarization of ferroelectric ceramic materials

A method of enhancement of output performance of TENGs by polarized ferroelectric material is widely investigated. As mentioned before, organic ferroelectric materials such as PVDF and its copolymer can increase the output performance of TENGs after poling process. Similarly, inorganic ferroelectric materials also affect the output performance of composites. Ferroelectric ceramic material with aligned dipole structure by polarization can increase the surface charge density, resulting in high output performance. **Figure 1.9a** illustrates non-aligned and aligned dipole orientation in TENGs before and after poling process.[62] These aligned dipole structure can obtain high surface potential, which can attract more negative charges from Al. **Figure 1.9b** also shows the effect of polarized ceramic material in the sponge structure TENGs. The output voltage and current are increased by ~50% after poling process.[63]

1.6. Research goal

As aforementioned, various researches to increase the performance of TENGs have been introduced by structural and material modifications. Although these TENG devices have achieved great outcomes to increase the triboelectric outputs, there are still problems to be solved. Conventional TENGs with ferroelectric materials such as PVDF and PVDF-TrFE have the advantage of controllable surface charge density by dipole alignment, which leads to high surface potential and thus improved triboelectric output. However, the organic-based triboelectric sensor[64] has a limited output performance due to relatively low dielectric constant. On the other hand, the TENGs with inorganic materials[65] possess high output performance due to high polarization caused by high dielectric properties and high permittivity, but their brittleness prevents their applications in flexible devices. The hybrid organic/inorganic materials with both properties of high dielectric materials and flexibility have been applied to high performance TENG devices. However, most of these TENGs have been demonstrated in the form of composites, resulting in the agglomeration of inorganic materials and thus preventing effective polarization by the mechanical stress.[66]

Here, we introduce multilayered ferroelectric organic/inorganic hybrid TENGs. Compared to composite-based TENGs, a multilayered structure can effectively transfer the vertical stress to inorganic nanoparticles, leading to the generation of greatly improved triboelectric output. In addition, introducing the poling process[67] helps to align the dipole in the multilayered ferroelectric materials and thus large surface potential, leading to an additional increase in triboelectric output. Based on the enhanced triboelectric performance, our TENG device can provide a great possibility for applications in energy harvesting devices, self-powered sensor, and acoustic sensor.

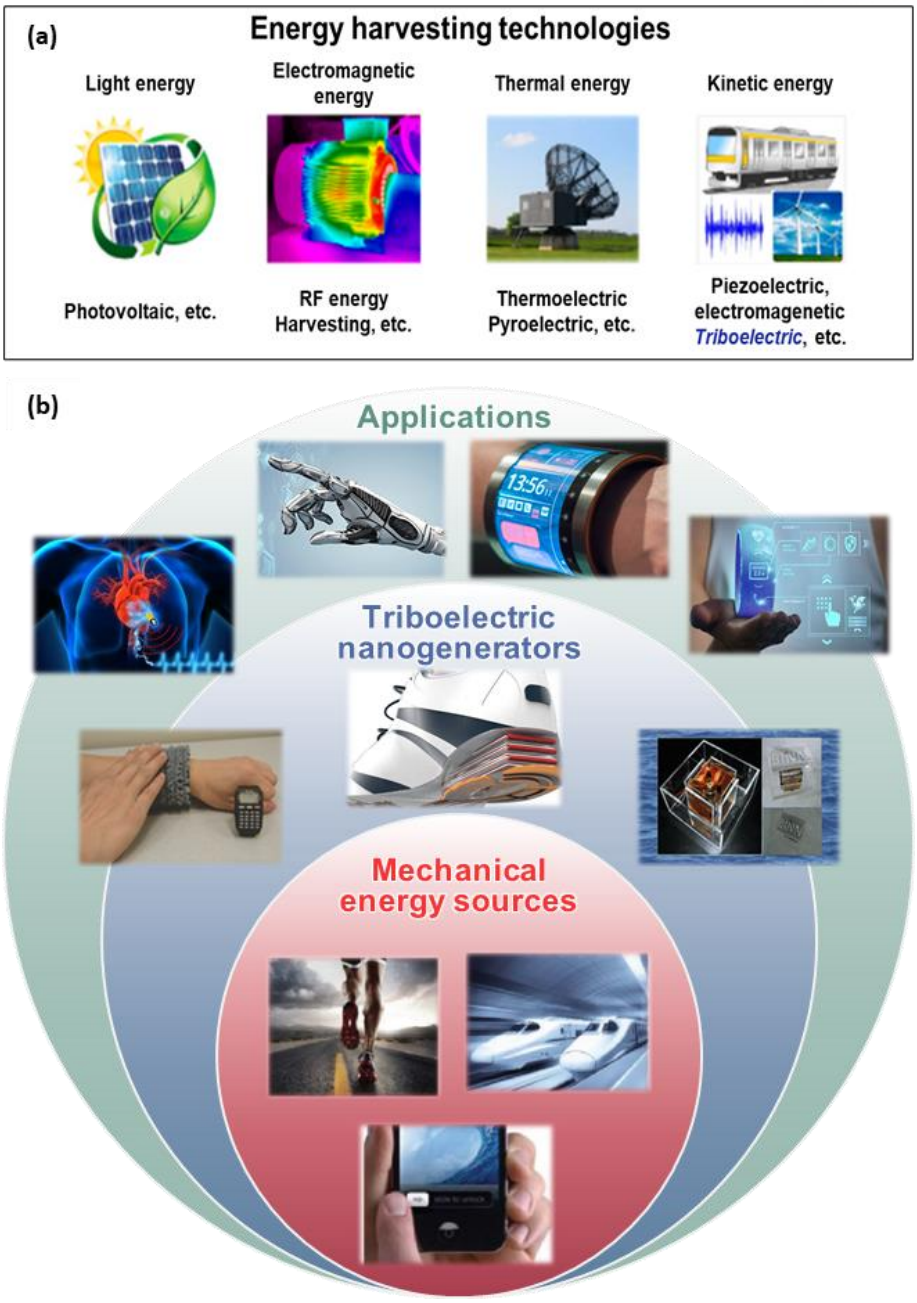

Figure 1.1. (a) Various energy harvesting technologies scavenging from light energy, electromagnetic energy, thermal energy, kinetic energy (Tang, X. et al. *Sensors.* **2018,** 18 (12), 4113). (b) The applications for wearable device, smart health-care system, self-powered energy system, and tactile sensor (top). The triboelectric nanogenerators with efficient structural design such as textile, multi-layer, 3D artifact based device (middle) (Niu, S. et al. Nature communications. **2015,** 6, 8975, Zhang, L. M. et al. Nano Energy. **2016,** 22, 87-94, Lai, Y. C. et al. Advanced Functional Materials. **2017,** 27 (1), 1604462). Various mechanical energy sources for triboelectric nanogenerators such as human motion, sliding and vibration (bottom) (Zheng, Q. et al. *Advanced Science.* **2017**, *4* (7), 1700029).

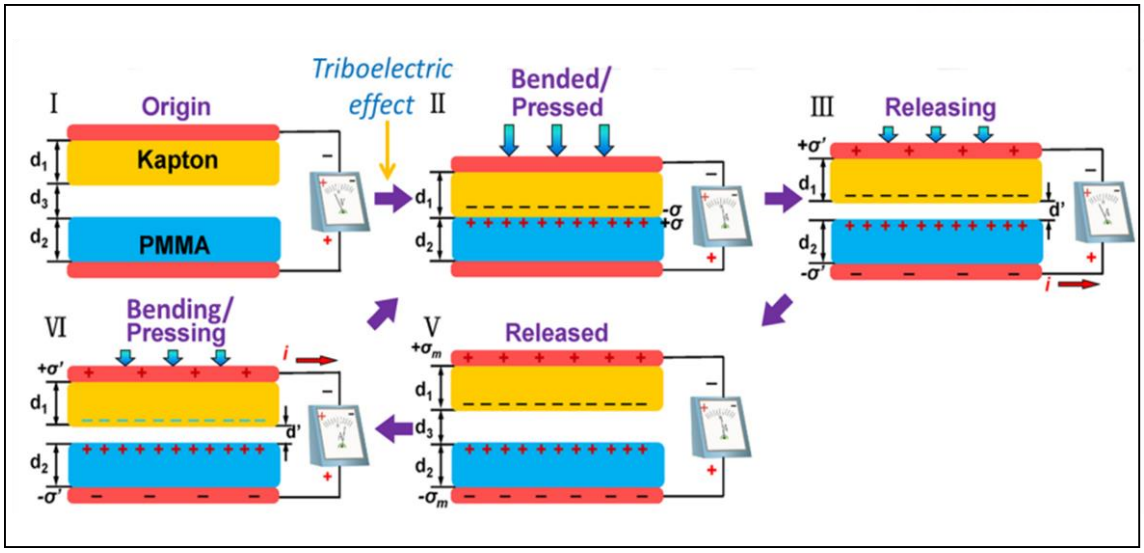

Figure 1.2. Schematics of working mechanism of triboelectric nanogenerator (I) Original states without external force. (II) Full contact between Kapton and PMMA film. (III) External forces are releasing and the two films are separated. (V) Two films are separated by a large gap distance. (VI) Two films are approaching. (Zhu, G. et al. *Nano letters*. **2012**,12(9),4960-4965)

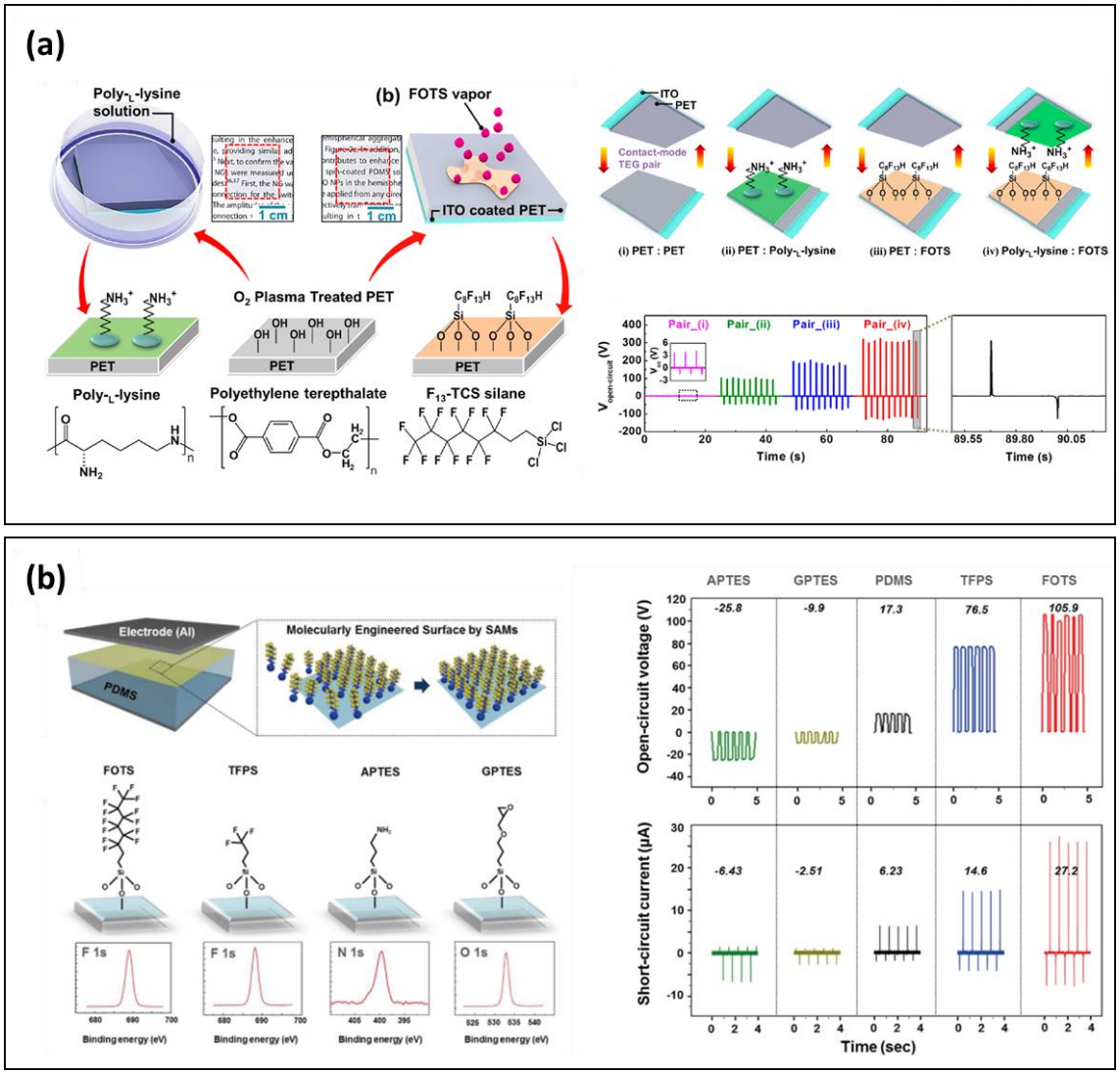

Figure 1.3. Surface functionalization to enhance the output performance of triboelectric nanogenerator. (a) The TENGs based on surface functionalized PET film using poly-L-lysine solution and FOTS vapor. (Shin, S-H. et al. *ACS Nano.* **2015,** *9* (4), 4621-4627) (b) The TENGs with modified surface from four different self-assembled monolayers (SAMs) such as APTES, GPTES, TFPS, FOTS. (Song, G. et al. *Chemistry of Materials* **2015,** *27* (13), 4749-4755)

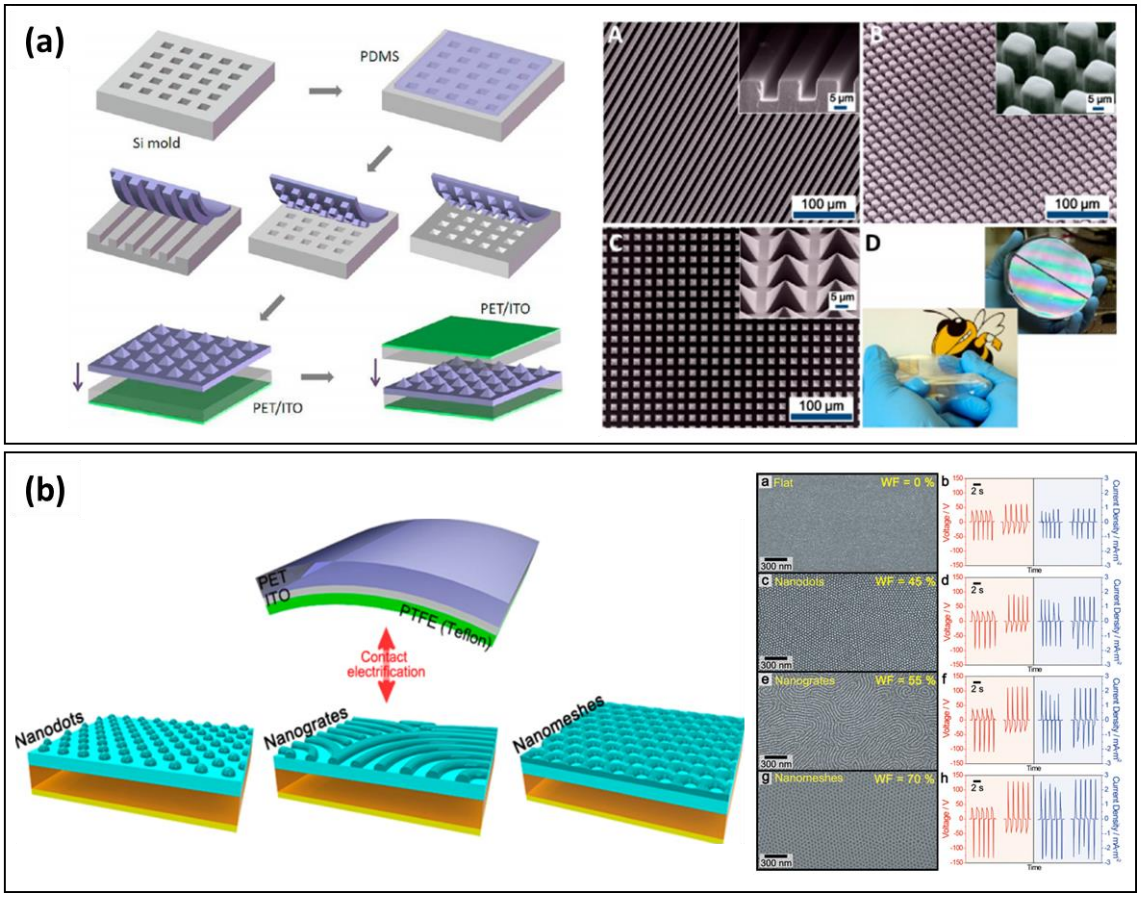

Figure 1.4. Surface morphology modification to improve the output performance of triboelectric nanogenerator. (a) Micro-patterned surfaces such as lines, cubics, pyramids. (Fan, F-R. et al. *Nano letters.* **2012,** *12* (6), 3109-3114) (b) Nano-patterned surfaces such as nanodots, nanogrates, and nanomeshes and improved output performance compared to flat surface of TENGs. (Jeong. C. K. et al. *Nano letters.* **2014,** *14* (12), 7031-7038)

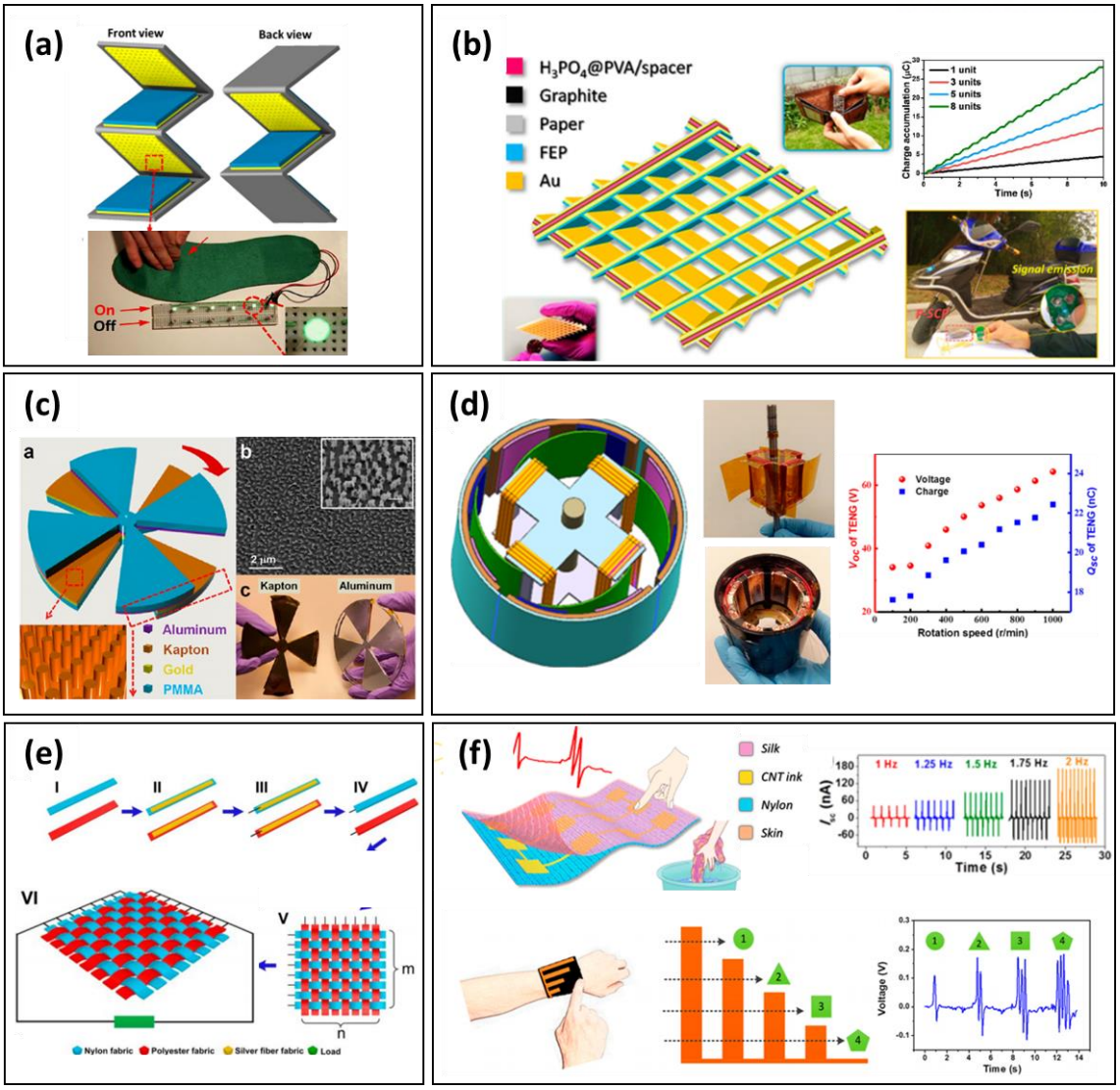

Figure 1.5. Various structural designs of triboelectric nanogenerator (a) Multilayered structure device (Zhu, g. et al. *Nano Energy.* **2013,** *2* (5), 688-692) (b) Ultralight paper-based rhombic-shaped TENGs (Guo, H. et al. *ACS nano.* **2017,** *11* (5), 4475-4482) (c) Disk-shape TENGs to utilize rotating energy (Lin, L. et al. *Nano letters.* **2013,** *13* (6), 2916-2923) (d) Freestanding mode TENGs with low friction force (Wang, P. et al. *ACS nano.* **2018,** *12* (9), 9433-9440) (e) Woven structured TENGs using commercial fabrics (Zhou, T. et al. *ACS applied materials & interfaces.* **2014,** *6* (16), 14695-14701) (f) Screen printed electronic textile based TENGs with striped and squared array (Cao, R. et al. *ACS nano.* **2018,** *12* (6), 5190-5196)

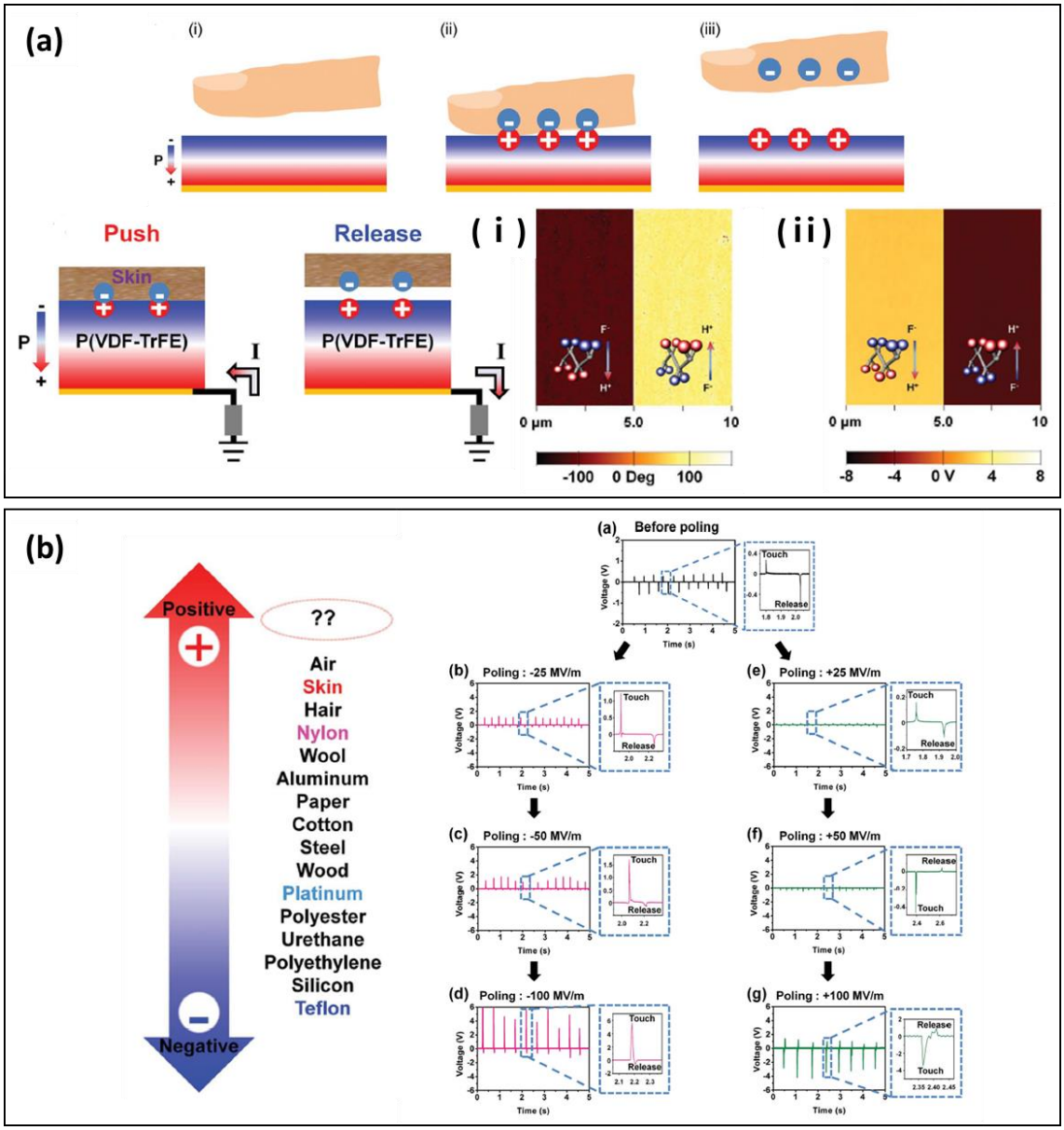

Figure 1.6. Control of triboelectric properties by polarization of ferroelectric material. (a) Schematic images of contact-separation process between human skin and poled PVDF-TrFE and a single electrode mode of TENGs. (i) PFM image of the PVDF-TrFE after negative and positive poling process without friction with skin. (ii) KPFM image of the surface of PVDF-TrFE (b) Triboelectric series and the output voltages of PVDF-TrFE with different poling drection and intensity. (Lee, J. H. et al. *Advanced materials* **2015,** *27* (37), 5553-5558)

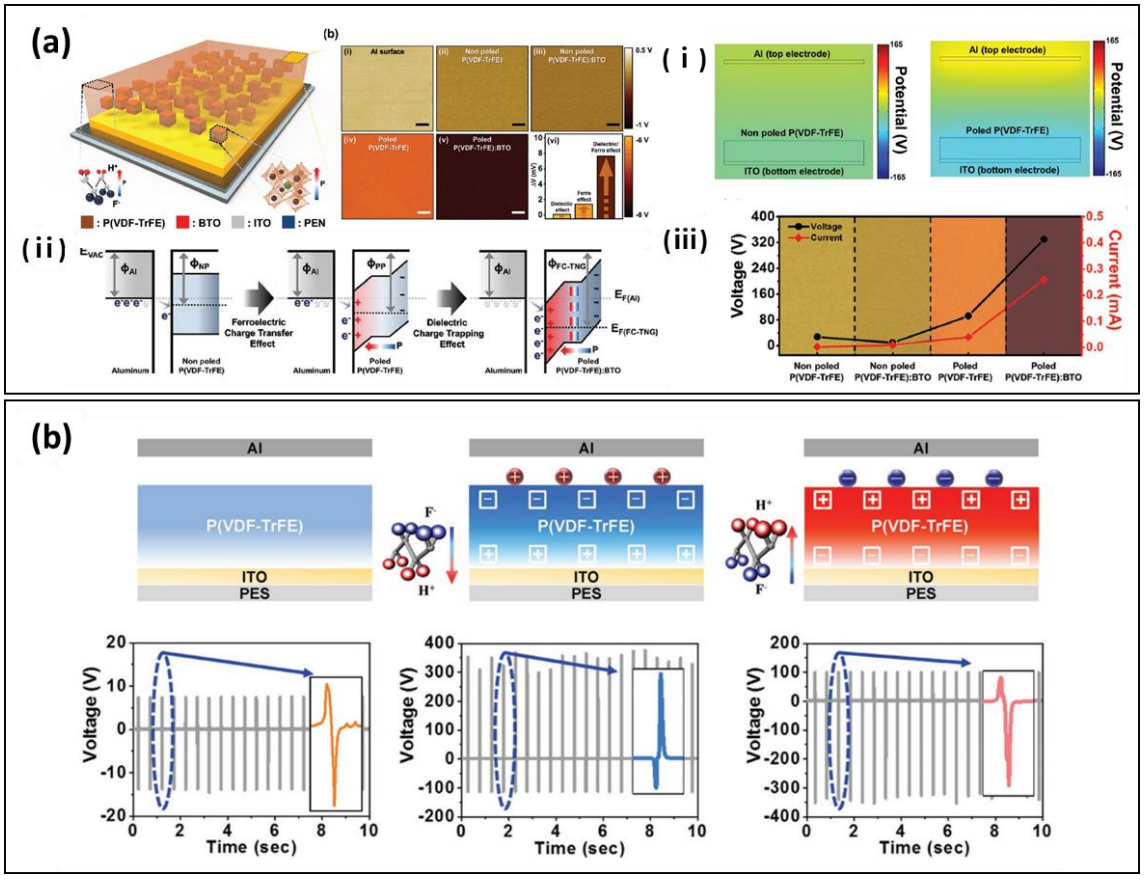

Figure 1.7. Enhancement of surface charge density by polarization of ferroelectric PVDF-TrFE. (a) The Schematic images of TENGs and (i) COMSOL multiphysics, (ii) Energy band gap diagram and (iii) Improved output performance of polarized PVDF-TrFE. (Seung, W. et al. *Advanced Energy Materials.* **2017,** *7* (2), 1600988) (b) The illustration and output voltages of non-polarized PVDF-TrFE, positively and negatively polarized PVDF-TrFE (Lee. K. Y. et al. *Advanced Functional Materials.* **2016,** *26* (18), 3067-3073)

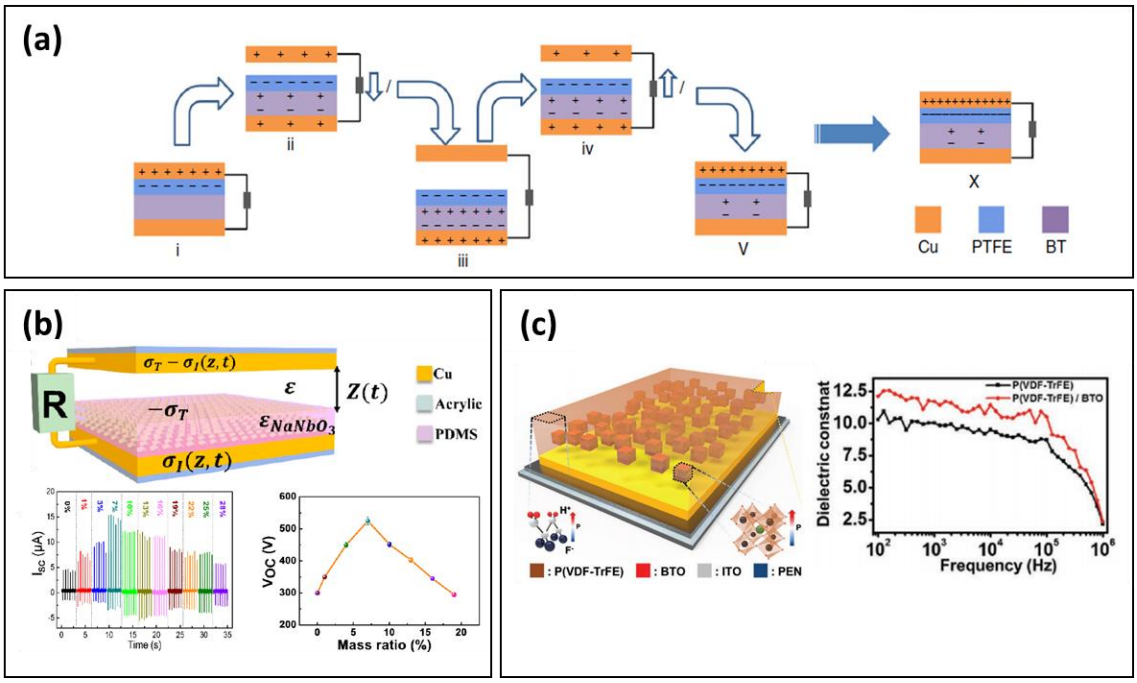

Figure 1.8. Ceramic/polymer composite type triboelectric nanogenerator to increase the output performance of system. (a) Working mechanism of TENGs consists of PTFE and BTO with high dielectric permittivity. (Wang, J. et al. *Nature communications.* **2017,** *8* (1), 88) (b) The schematic images of $NaNbO_3$/PDMS composite and output performance under different concentrations of $NaNbO_3$ (Lai, M. et al. *Journal of Physics D: Applied Physics.* **2017,** *51* (1), 015303) (c) The illustration of PVDF-TrFE/BTO composite based TENGs and increased dielectric constant of composite. (Seung, W. et al. *Advanced Energy Materials.* **2017,** *7* (2), 1600988)

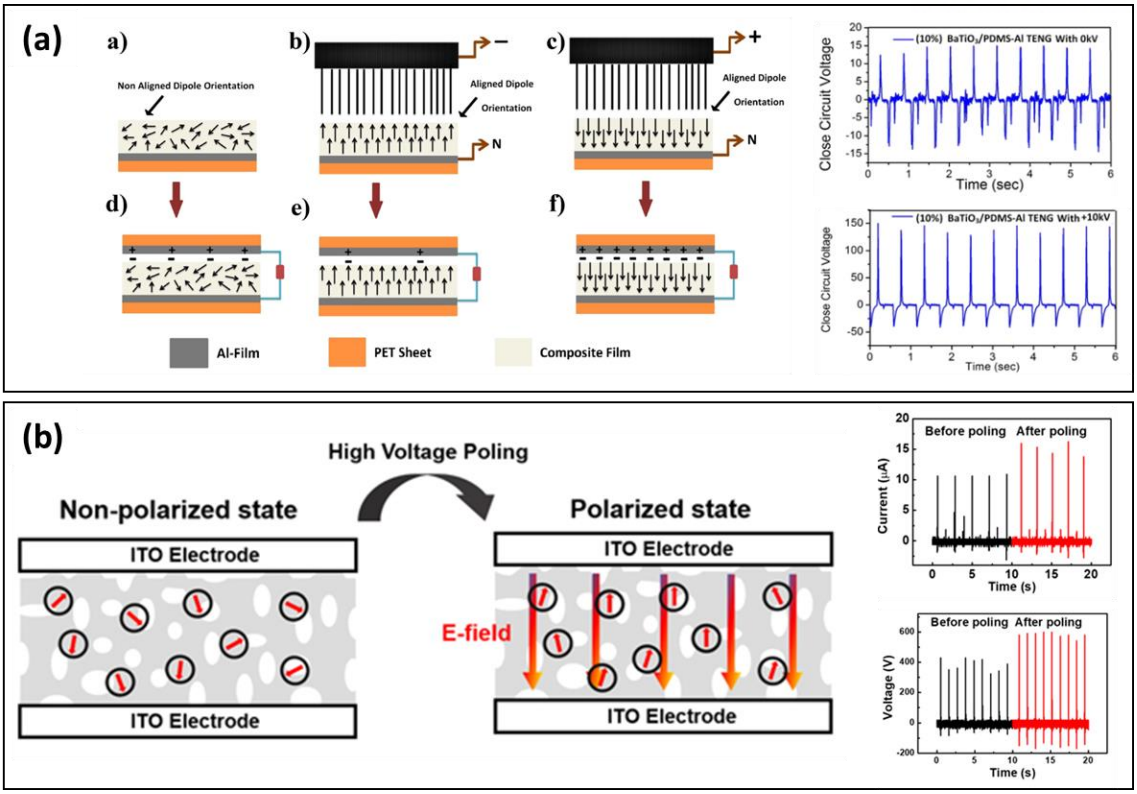

Figure 1.9. Improve the output performance of polymer/ceramic composite film through polarization of ferroelectric ceramic material. (a) Schematic images of non-aligned and aligned dipole orientation of $BaTiO_3$ during poling process and increased output voltage (Ali, D. et al. *Nanotechnology* **2017,** *28*(7), 075203) (b) Schematic image of non-polarized and polarized state TENGs with sponge structure. The enhanced output current and voltage of TENGs before and after poling process. (Park, D. et al. *Nanotechnology* **2018,** *29* (18), 185402)

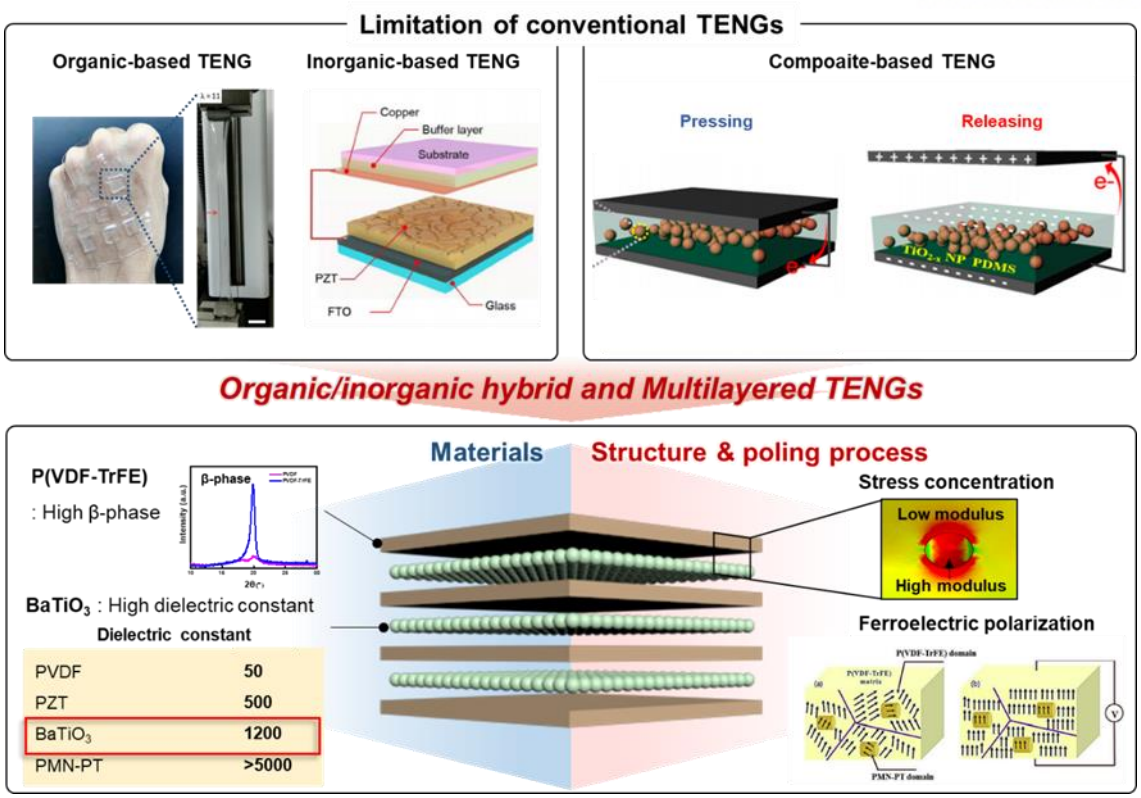

Figure 1.10. Highly enhanced output performance of multi-layered ferroelectric organic/inorganic hybrid TENGs (Pu, X. et al. *Science advances.* **2017,** 3 (5), e1700015, Su, L. et al. *Nano Energy.* **2017,** 31, 264-269, Park, H.-W. et al. *Micromachines.* **2018,** 9 (8), 407, Yaqoob, U. et al. *Composites Part B: Engineering.* **2018,** 136, 92-100)

2. Experiments

2.1. Preparation of materials

The $BaTiO_3$ nanoparticles (BTO NPs) coated with polyvinylpyrrolidone (PVP) (average size of 200 nm) were purchased from U.S. Research Nanomaterials, Inc. The Poly(vinylidenefluoride-co-trifluoroethylene) (70/30) powder was obtained from Piezotech, France. The PVDF-TrFE powder (2 g) was dissolved in N,N-dimethylformamide (DMF) solvent (8 g) to make 20 wt% solution. The PVDF-TrFE/DMF solution was stirred for 2 h under heating at 40 °C for uniform distribution. The PVP coated BTO NPs powder (0.31 g) was dispersed in EtOH (10 g) to make 3 wt% using bath-sonication for 1 h. The PVP coated BTO NPs were prepared to get uniform dispersion of nanoparticles in EtOH.[68]

2.2. Fabrication of PVDF-TrFE/$BaTiO_3$ multilayered film

The PVDF-TrFE/DMF (20wt%) solution was coated onto the Cu electrode using bar coater with a coating speed of 6 mm/sec. The standard Meyer rods RSD 3 (RD Specialties, Inc.) which its diameter is 76 μm was used. To control the thickness of the films, PI tapes were rolled onto the Meyer rod. The controlled thickness of PVDF-TrFE film is measured approximately 10 μm. After coating, the films were dried for 30 min at 35 °C to reduce the surface roughness and then for 30 min at 60 °C to remove the remaining DMF as the solvent. The $BaTiO_3$-PVP/EtOH suspension was coated onto the PVDF-TrFE coated Cu electrode using bar coater with the same coating speed. The Meyer rod RSD 2 which its diameter is 51 μm was used. After that, the coating and drying process of PVDF-TrFE were repeated one more time. Then the sandwich structured PVDF-TrFE/$BaTiO_3$ films were fabricated. To make multilayered PVDF-TrFE/$BaTiO_3$ film, this fabrication process was repeated. Then, the film was annealed at 140 °C for 2 h. To align the dipole of ferroelectric material, an electric field of 30 MV/m was applied to the sample at 80 °C.

2.3. Characterization of material and device

All experiments were performed under ambient condition. The crystallinity of the PVDF-TrFE film and $BaTiO_3$ NPs were characterized using X-ray diffraction (XRD) and the morphologies of PVDF-TrFE/BTO multilayered film were investigated by field emission scanning electron microscopy (FE-SEM S-4800, Hitachi). Fourier transform infrared (FT-IR) measurement was used for the crystal structure conversion of β-phase PVDF-TrFE film. TGA analysis was

examined for measurement of $BaTiO_3$ concentration inside PVDF-TrFE/BTO multilayered film. The triboelectric output voltage and current were measured using an oscilloscope (DPO 2022B, Tektronix, US), source meter (2450-SCPI, Keithley, US), respectively. Vertical pressure was applied by the pushing tester (JIPT, JUNIL TECH, Korea). The area of the contact surface is 1 cm^2.

3. Results and Discussions

3.1. Fabrication of multilayered organic/inorganic hybrid triboelectric nanogenerator

A **s**chematic of the fabrication process for multilayered hybrid triboelectric nanogenerators based on PVDF-TrFE/BTO NPs films is shown in **Figure 3.1a**. The multilayered films are fabricated by repetitive bar-coating process of PVDF-TrFE solution and BTO NPs-dispersed solution alternatively and annealing process. In multilayered film, each PVDF-TrFE layer shows the regular thickness of approximately 10 μm the PVDF-TrFE. In addition, the tetragonal-structured BTO NPs (200 nm) with a concentration of 3 wt% are located onto the surface of PVDF-TrFE film. For constructing TENG devices, additionally the top (aluminum) and bottom (copper) electrodes are used. The Al foil acts as a top electrode and positive triboelectric material since it easily loses its electrons during friction. To enhance the triboelectric property, we additionally treated the post electrical poling process, which aligned the inner dipole of ferroelectric PVDF-TrFE polymer and BTO NPs, and thus increasing the surface potential (**Figure 3.1c**).

For examining the ferroelectric PVDF-TrFE polymer and BTO NPs, we analyzed the crystalline structures and phases by XRD and FT-IR measurements. **Figure 3.2a** shows the XRD patterns of the PVDF-TrFE ranging from 15° to 30°. A single peak is observed at an angle of 2θ at approximately 19.8°, corresponding to the ferroelectric β-phase of PVDF-TrFE. In addition, **Figure 3.2b** shows XRD result indicating that the PVP-coated BTO NPs have a good crystalline structure with a ferroelectric tetragonal phase.[53] **Figure 3.3** exhibits FT-IR analysis of the PVDF-TrFE and PVDF-TrFE/BTO film.[69, 70] In the PVDF-TrFE film and PVDF-TrFE/BTO film, we can observe three strong peaks of 850 and 1288 cm^{-1} (CF_2 symmetric stretching), and thus 1400 cm^{-1} (CH_2 wagging vibration). It indicates that both films have strong β-phase crystals after annealing process.

3.2. Improvement of triboelectric performance by ferroelectric film

Ferroelectric materials with controllable polarization by electrical poling process can improve the triboelectric performance by modulation of the surface potential. To study the effect of poling process on the surface potential, we prepared single-layered PVDF-TrFE films before and after poling process **(Figure 3.4a)**. Initial ferroelectric PVDF-TrFE with β-phase has permanent dipole moments, leading to high surface potential. However, because the dipoles of PVDF-TrFE are partially orientated in non-poled state, the sum of all dipole moments is irregular. When an electric field of 30 MV/m is applied, the molecules are aligned according to the direction of applied electric field. The increase in aligned dipoles creates the high surface potential in PVDF-TrFE film, which leads to the enhanced surface charge density. As shown in **(Figure 3.4b)**, the current and voltage of poled PVDF-TrFE films are enhanced by approximately 2 times compared to non-poled PVDF-TrFE films.

3.2.1. Effect of dielectric $BaTiO_3$.

The BTO NPs with high dielectric permittivity additionally enhances the ferroelectric polarization under electrical poling process. To verify the BTO NPs-induced high ferroelectric polarization, we compared the triboelectric properties depending on the introduction of BTO NPs. As shown in **Figure 3.5a**, we prepared single layer PVDF-TrFE films with and without BTO NPs interlayers. Under applied pressure of 98 kPa, the PVDF-TrFE with BTO interlayer exhibits the increased triboelectric current and voltage compared to the one without BTO interlayers.

To acquire the optimized output performance of the PVDF-TrFE with BTO interlayer, we compared the triboelectric properties depending on the concentration of the BTO NPs. The different BTO NPs concentration can be controlled by the coating cycles of the BTO/EtOH solutions with BTO concentration of 1 wt% and 3 wt%. Since the BTO/EtOH solution is supersaturated over 3 wt%, we coated BTO NPs on the surface multiple times using 3 wt% solution to obtain the high surface density of BTO NPs. **Figure 3.6a** shows the optical microscope (OM) images exhibiting different surface density of BTO NPs on the PVDF-TrFE film. **Figure 3.6b** shows the average output current and voltage of the single PVDF-TrFE film with BTO interlayer. The PVDF-TrFE film with BTO interlayer coated with 3 wt% BTO/EtOH solution by one time (sample b) exhibits the optimized output performance with a small standard deviation compared to twice and three times coated BTO layers. Since there is no significant enhancement in the triboelectric output performance over one cycle coating process, we fixed the BTO concentration with one cyclic coating of 3 wt% BTO solution for the fabrication of our triboelectric nanogenerator systems.

3.2.2 Working principles of single-layered ferroelectric PVDF-TrFE/BTO NP films

Based on the experimental results, we illustrate the effects of the ferroelectric materials on the triboelectric performance as shown in **Figure 3.7a.** Due to the electrical poling process, the ferroelectric PVDF-TrFE and BTO NPs align inner dipoles in one direction, increasing the surface potential. Once the pressure is applied on the film, the oriented dipoles of BTO establish a positive piezoelectric potential, resulting in additional increase in the surface potential in the film. Caused by enhanced surface potential difference, negative charges of the Al surface more efficiently transfer to the PVDF-TrFE/BTO film and thus increase the surface charge density of TENGs.

The working mechanism of TENGs based on PVDF-TrFE/BTO film is illustrated in **Figure 3.7b**. The working principle is based on the triboelectric effect and electrostatic induction. The periodic contact-separation process leads to charge flow between the top and bottom side of the electrode through the external circuit. When two materials with different triboelectric properties are in contact with each other, the opposite charges are formed on each surface of material due to triboelectric effect. Al is positively charged by losing electrons and the PVDF-TrFE/BTO films are negatively charged by attracting electrons. When two materials are separated, a potential difference appears between two materials. To maintain the electrostatic equilibrium, the induced free charges flow through the external circuit between the top and bottom electrodes. This flow continues until neutralized. When two materials are closed again, the triboelectric potential difference disappears and the free electron flow back into the circuit.

3.3. Improvement of triboelectric performance by a multilayered structure

In addition to the effect of ferroelectric material on the triboelectric performance, the multilayered structure can be expected to improve the triboelectric properties due to synergetic triboelectric potential. To verify the structural effect on the triboelectricity, we investigated the dependence of the number of stacking layers on the triboelectric property. **Figure 3.8** shows the output current and voltage of the multilayered PVDF-TrFE film with and without BTO interlayer according to different numbers of stacking layers from 1 to 7 layers. In case of multilayered PVDF-TrFE film without BTO interlayer, triboelectric outputs are increased up to 4-layered films, and then the signals are saturated up to 7-layered films. The four-layered film shows the maximum output performances with voltage of 27.2 V, and current of 0.9 μA, respectively (**Figure 3.8c and 3.8e**). The output performances of multilayered PVDF-TrFE films with BTO interlayer display a similar behavior with multilayered PVDF-TrFE films. The output performance of multilayered film with BTO increased up to 4-layered film, and then saturated up to 7-layered film. The multilayered PVDF-TrFE/BTO film shows the maximum output current of 1.92 μA and voltage of 45.7 V in the 4-layered film (**Figure 3.8d and 3.8f**). The output performance of all of the multilayered PVDF-TrFE film with BTO interlayer ranging from 1 to 7 are higher than those of multilayered PVDF-TrFE film without BTO interlayer.

To further investigate the effect of ferroelectric polarization in multilayered films, we prepared a 4-layered PVDF-TrFE/BTO film under three different polarization conditions (**Figure 3.9a**). Depending on the direction of polarization, the surface potential properties are alternatively changed. The PVDF-TrFE with positive surface potential has more negative triboelectric properties than non-poled PVDF-TrFE in the triboelectric series, resulting in attracting more charges from Al **(Figure 3.9c).** The PVDF-TrFE with negative surface potential exhibits positive triboelectric properties compared to Al. As a result, the negatively polarized PVDF-TrFE loses the electron from Al. Therefore, the output signals of negatively polarized PVDF-TrFE show the opposite tendency compared to non-poled and positively polarized PVDF-TrFE (**Figure 3.9d)**

3.3.1 Systematic investigation of multilayer effect on triboelectric properties

For systematic study of multilayer effect on triboelectric properties, we prepared four different types of samples: single PVDF-TrFE, multilayered PVDF-TrFE, single PVDF-TrFE/BTO composite, and multilayered PVDF-TrFE/BTO films. All samples have the same thickness as the one with 4 multilayer film (~50 μm) **(Figure 3.10a).** The multilayered film can be fabricated by stacking the layers. The single film is made by one-time coating process with the same thickness of multilayered film. The BTO concentration of single PVDF-TrFE/BTO composite is similar to

that of the multilayered PVDF-TrFE, where the concentration of BTO inside PVDF-TrFE matrix is measured by thermogravimetric analysis (TGA) (**Figure 3.10d**).

In **Figure 3.10b and 3.10c**, we observe the average output current and voltage of PVDF-TrFE film with the structure of a single composite and multilayer (red region) and PVDF-TrFE/BTO film with the structure of a single composite and multilayer (blue region). A multilayered film of PVDF-TrFE/BTO film has the output current of 1.77 μA and voltage of 44.5 V, while the single film has the output current of 1.2 μA and voltage of 35.4 V. The output current of multilayered PVDF-TrFE/BTO film are increased up to 47 % compared to single composite film with the same concentration of BTO NPs. This is attributed to the relatively easy aggregation of BTO NPs in the single PVDF-TrFE/BTO composite film. In addition, the BTO NPs exposed to the surface in the single composite induce the reduction of surface contact area in response to mechanical pressure. On the other hand, the multilayer type TENGs use the BTO NPs dispersed in EtOH solution compared to composite with directly mixed BTO NPs in polymer matrix, which reduces the aggregation between the BTO NPs. In addition, the multilayer type TENGs does not expose the BTO NPs on the surface.

Another reason can be explained by the effect of the horizontal alignment of the BTO NPs in the multilayer structures. The merit of multilayered structure is that the vertical stress is effectively transferred to BTO NPs due to their horizontally aligned structure of BTO NPs inside PVDF-TrFE matrix. Compared to randomly orientated BTO NPs in composites without multilayer structures, the BTO NPs aligned along one direction in the multilayers efficiently produce the piezoelectric potential, which affects the surface potential in the PVDF-TrFE/BTO film.[71-73]

To verify our suggestion on the effect of aligned BTO NPs, the piezoelectric properties of the above four types of sample are examined. The bottom surface of the film is coated on the Cu electrode, and the top surface of film is deposited with Pt electrode. In case of piezoelectric nanogenerators, the ferroelectric films with oriented dipoles produce the piezoelectric potential under external pressure, which can flow electrons between two electrodes to balance the piezoelectric potential difference. **Figure 3.11b** exhibits the output current of the piezoelectric nanogenerators with four different samples. The PVDF-TrFE films including the BTO NPs exhibit higher output performance than the PVDF-TrFE films without BTO NPs due to the high dielectric constant of BTO NPs. The single and multilayer PVDF-TrFE films display similar output values. On the other hand, the multilayer PVDF-TrFE/BTO film shows a higher output performance of approximately 8 nA than the outputs of single PVDF-TrFE/BTO film (~1 nA). Since there is no significant difference in outputs between single and multilayer PVDF-TrFE films, the enhanced output value of multilayer PVDF-TrFE/BTO film is originated by BTO NPs. From these results, we found that the horizontally aligned BTO NPs enhance the piezoelectric potential

in the multilayered film. Under the same external force, the horizontally aligned BTO NPs are effectively affected by the applied stress compared to randomly dispersed BTO NPs, resulting in the creation of a high piezoelectric potential in the film. Therefore, the multilayer PVDF-TrFE/BTO film has the maximum piezoelectric performance.

3.4. Performances of triboelectric nanogenerators based on multilayered ferroelectric films

To investigate the electrical performance of TENGs, we analyzed the output performance of TENGs according to forward and reverse connection modes. **Figure 3.12** shows the schematic images of forward and reverse connection modes, which resulted in the opposite peak signals of forward and reverse connection modes of TENGs with the same intensity. In the forward connection modes, the positive and negative signals were observed during contact-separation process. Meanwhile, the reverse connection modes results in the opposite direction of negative and positive signals. Based on this result, we found that the measured electrical current and voltage truly comes from triboelectric effects of materials.

Based on optimized multilayered ferroelectric films, we further investigated the energy harvesting performance of triboelectric nanogenerators. **Figure 3.13a and 3.13b** shows the comparison of the output current and voltage between non-poled and poled 4-multilayered films. The triboelectric property of the polarized multilayered film is significantly increased, where the maximum output current of 2.18 μA is about 10 times higher current value than the output current (210 nA) of the non-polarized multilayered film **(Figure 3.13a).** In addition, the output voltages of 6 V and 47.2 V are observed in the non-poled and poled film, respectively **(Figure 3.13b).** This enhanced output value can be attributed to the large surface potential induced by the well-aligned dipole in the polarized ferroelectric material.

To evaluate the power generation depending on the mechanical pressure, we measured the output voltage and current of the multilayered PVDF-TrFE/BTO film with post-poling process under different loading pressures. Under the application of mechanical pressure with constant frequency of 2 Hz, the output voltage is gradually increased with the sensitivity of 1.14 V/kPa (< 6.89 kPa) and 0.22 V/kPa (> 6.89 kPa) **(Figure 3.13c)**. In addition, the output currents increased with the pressure sensitivity of 48.7 nA/kPa (< 9.8 kPa) and 10.1 nA/kPa (> 9.8 kPa) **(Figure 3.13d).**

To find out the optimized output power density of TENGs, the output current and voltage are measured under different loading resistance, ranging from 1 KΩ to 750 MΩ. As displayed in **Figure 3.14a**, the current signals are decreased and the voltage is increased with increasing load resistance. As a result, the output power density reached the maximum value of 29.4 μWcm^{-2} at a load resistance of 100 MΩ (**Figure 3.14b**). For practical applications of the TENGs, we examined to power up light-emitting devices (LEDs) by the harvested energy. We connect a commercial rectifier to the TENGs to convert the AC voltage into a DC voltage output. The commercial green emission LEDs interlock to the rectifier connected the TENGs. The rectified output voltage is displayed in the inset of **Figure 3.14c**. Under periodic vertical force, it can be seen that commercial LEDs turns on the green lights through the rectified electricity.

3.5. Application of multilayered TENGs for frequency selective acoustic sensors

To further demonstrate the potential application of multilayered TENGs, we used our TENGs for self-powered acoustic sensors with frequency selective sensing capability. Since the multilayered film can control the thickness by simple fabrication process, the device can provide the frequency selectivity depending on the thickness of the film. Furthermore, its thin film structure is capable of oscillating by the low acoustic energy. Therefore, our multilayered PVDF-TrFE/BTO film is beneficial for acoustic sensing applications. **Figure 3.15a** illustrates the structural design of acoustic sensor consists of multilayered PVDF-TrFE/BTO film with sputtered Pt layer and ITO/PET film as the top and bottom electrodes. The triboelectric outputs are achieved by contact and separation between ITO and multilayered films. The PI tape as a spacer is attached to each side of the film to separate the two contact surfaces. We prepared 1-, 3-, 5- multilayer films with thickness of approximately 20, 40, 60 μm. respectively. **Figure 3.15b** shows the photograph of an acoustic sensor. The sound source is applied by a speaker with 98 dB in the frequency range from 100 Hz to 20 kHz, and the distance between the device and speaker is fixed at 1 cm. We analyzed the characteristics of acoustic sensors using triboelectric signals that is generated from the vibration of films through the applied acoustic energy (**Figure 3.15c)**.

Figure 3.16a exhibits the electrical properties of acoustic sensors according to thickness of films. The three types of sensors have an average output voltage of approximately 15 mV, which is higher than those of other acoustic sensors using piezoelectric effect. It is attributed to the high power density of triboelectric effect. To investigate the frequency selectivity of our acoustic sensors, we convert the electrical output from the time domain signal to the frequency domain signal by fast Fourier transform (FFT) analysis **(Figure 3.16b).** A single-layered film has the largest peak at 20 kHz and five-layered film shows the largest intensity at 0.4 kHz. The largest peak shift to lower frequencies as the thickness of film increases. This result can be attributed to different oscillation behavior of multilayered films depending on the thickness. The oscillation of each film is excited at certain frequency due to the harmonic oscillation phenomenon. In other word, the film with different thickness responds to the different resonance frequency. Therefore, our multilayered film can achieve the frequency selectivity by controlling the thickness. In addition, the acoustic sensitivity dependent on the number of multilayers can increase the difference in the generated outputs from each harmonic oscillation frequency, leading to improved frequency selectivity. Overall, we observed that the thin film TENGs-based acoustic sensors exhibit high intensity and large frequency response range, ranging from 100 Hz to 20 kHz. In addition, the frequency selectivity by controlling the thickness of the film can be available for various applications such as noise canceling technology and voice security system.

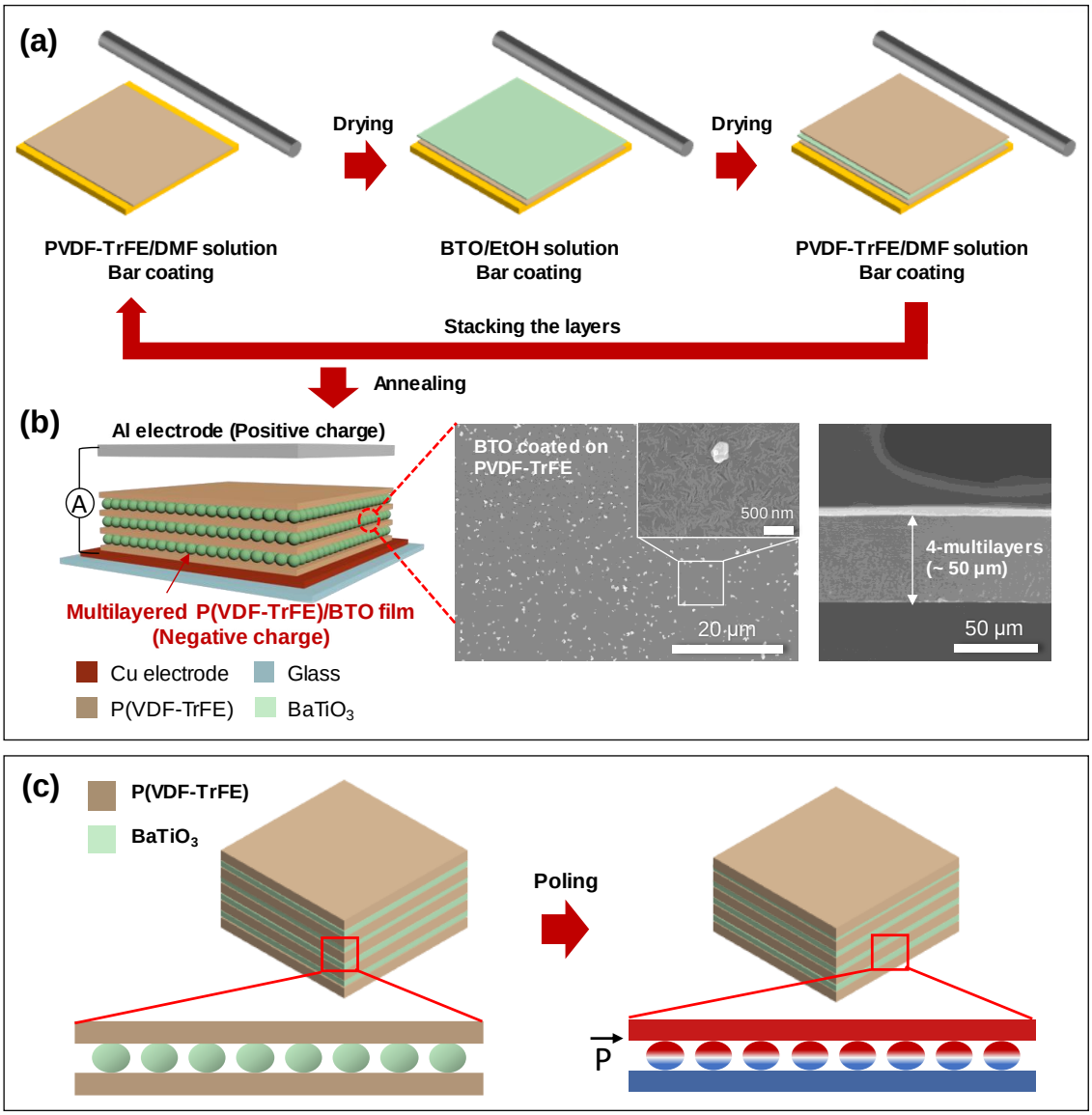

Figure 3.1. (a) Schematic for the fabrication process of the multilayered PVDF-TrFE/BTO film. (b) Schematic of a multilayered PVDF-TrFE/BTO based TENGs and SEM images of BTO coated on the PVDF-TrFE (left), and cross-sectional image of four-layered film. (c) Illustration of the multilayered PVDF-TrFE/BTO film before and after poling process.

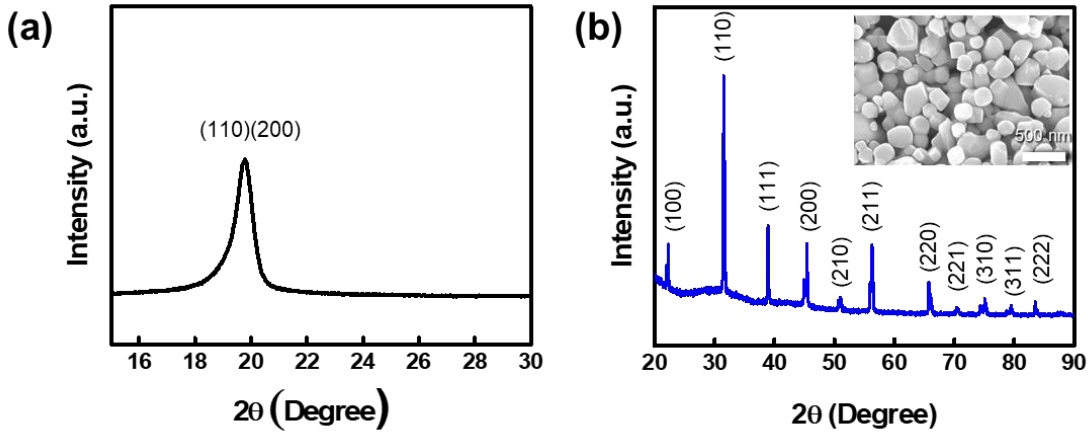

Figure 3.2. (a) X-ray diffraction (XRD) result of the PVDF-TrFE film with strong β-phase (110/200) (b) XRD patterns of the tetragonal BTO NPs. The inset displays SEM image of PVP-coated BTO NPs.

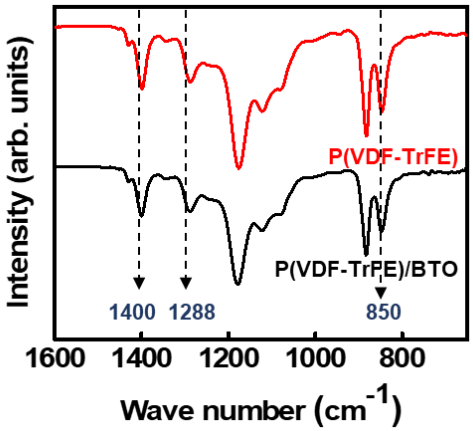

Figure 3.3. FT-IR spectrum of PVDF-TrFE and PVDF-TrFE/BTO film.

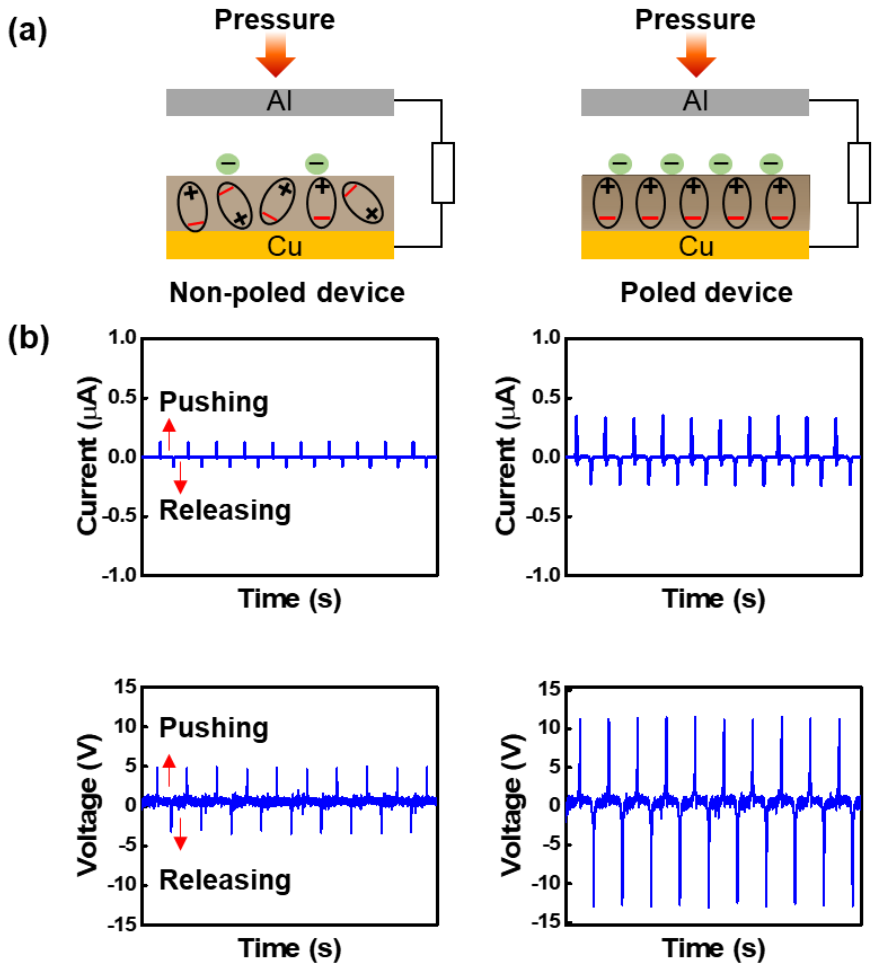

Figure 3.4 (a) Schematics of the TENGs with non-polarized and polarized state. (b) Output current and voltage of the two types of TENGs with non-poled and poled PVDF-TrFE film.

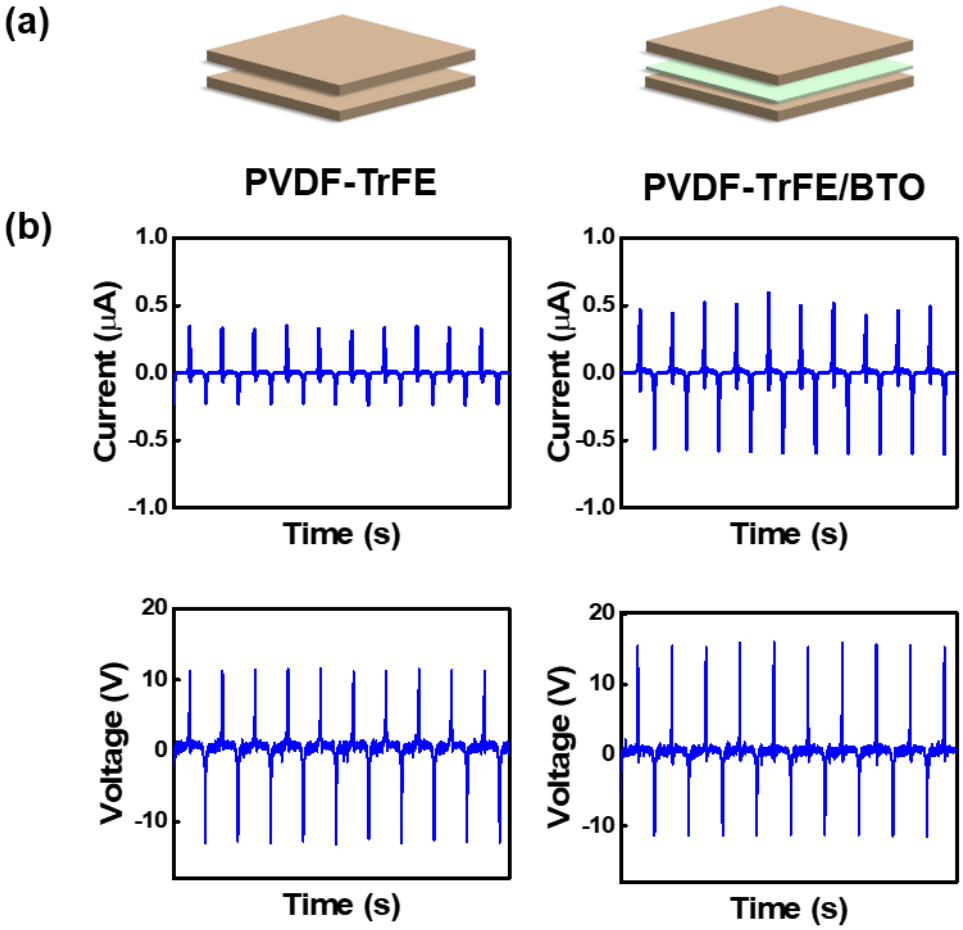

Figure 3.5 (a) Schematics of the PVDF-TrFE film without BTO NPs and the PVDF-TrFE/BTO film with dispersed BTO NPs between the two PVDF-TrFE layers. (b) Output current and voltage of the PVDF-TrFE film and the PVDF-TrFE/BTO film.

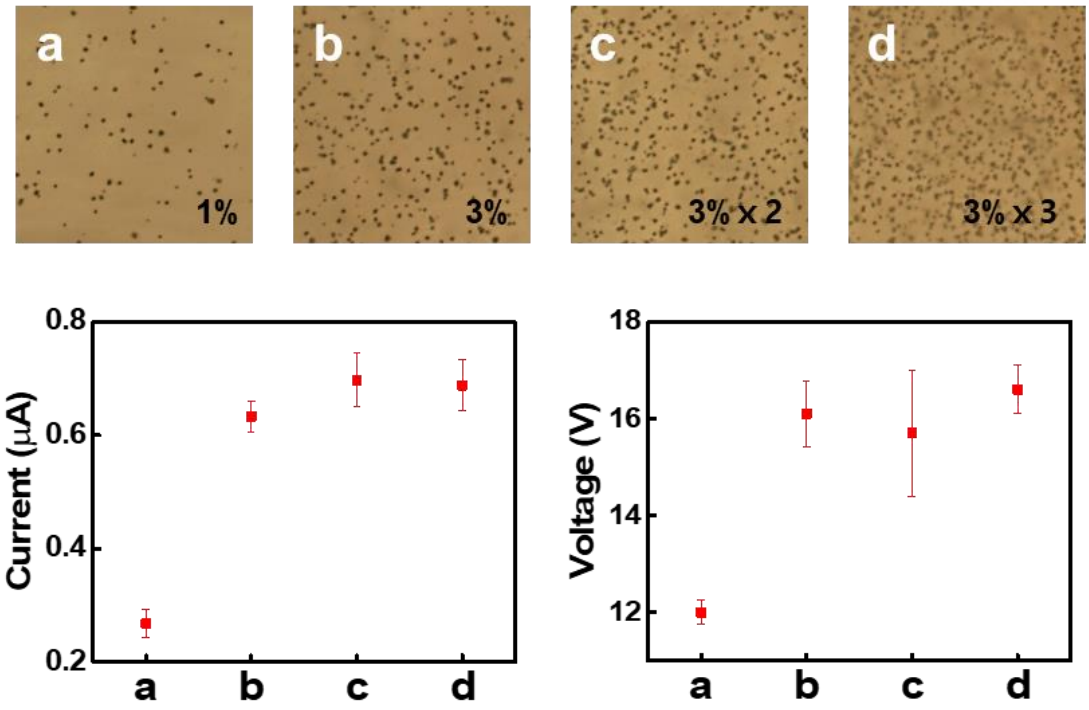

Figure 3.6. Schematic of BTO coated on the PVDF-TrFE with different concentrations of BTO/EtOH solution and output current and voltage of the single PVDF-TrFE and BTO interlayer.

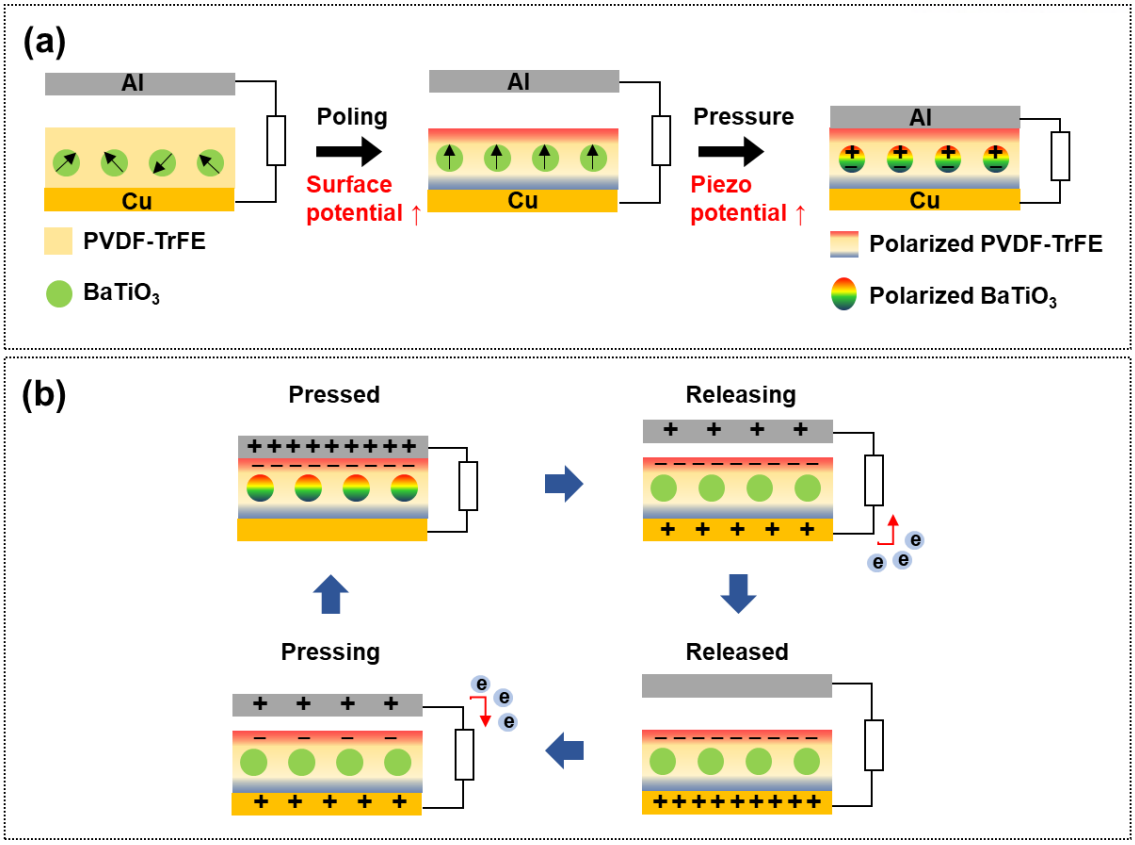

Figure 3.7. (a) Schematics of the working principle in the polarized PVDF-TrFE/BTO film. (b) Working mechanism of the TENG with polarized ferroelectric materials.

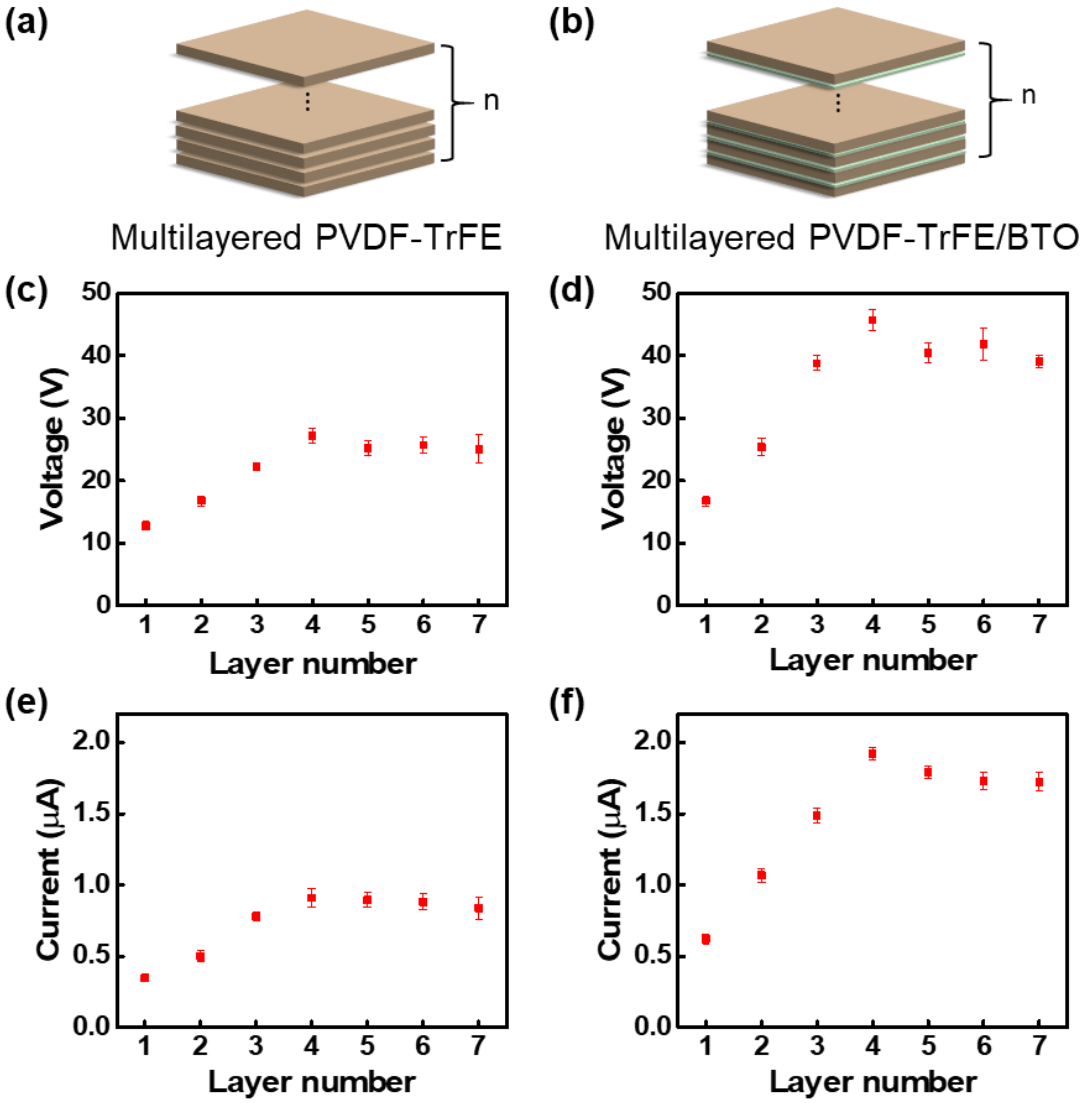

Figure 3.8. Schematics of (a) the multilayered PVDF-TrFE film and (b) the multilayered PVDF-TrFE/BTO film. The output voltage and current of (c and e) the multilayered PVDF-TrFE and (d and f) the multilayered PVDF-TrFE/BTO film at different number of layers, ranging from 1 to 7.

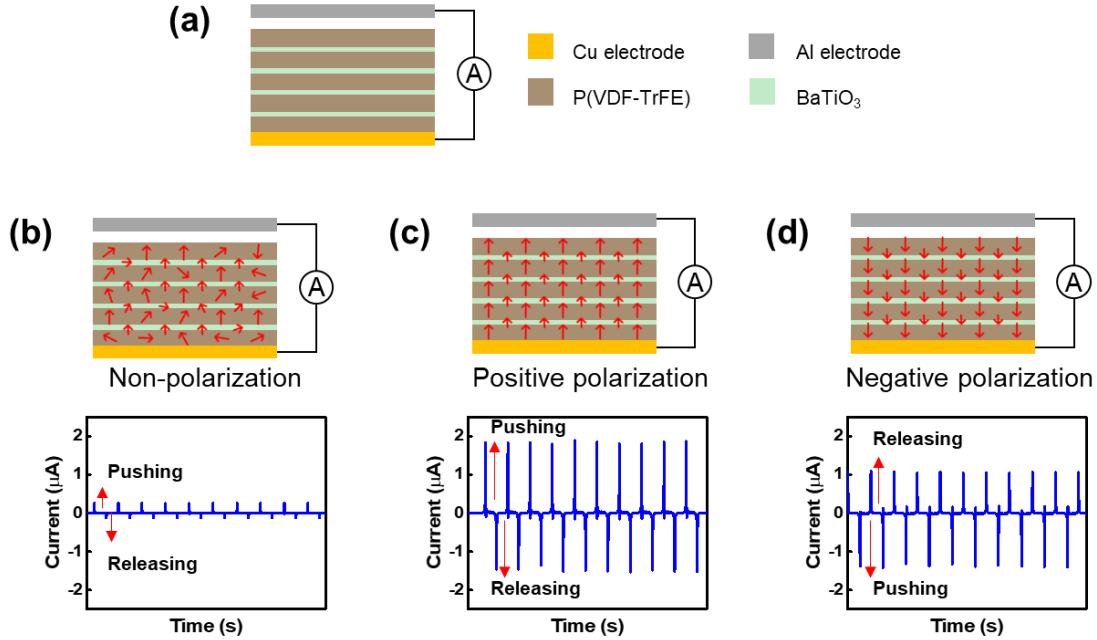

Figure 3.9. (a) Schematics of the four-layered PVDF-TrFE/BTO film based TENGs. Schematics and output current of the four-layerd PVDF-TrFE/BTO film with (b) non-polarization state (c) positive polarization state (d) negative polarization state.

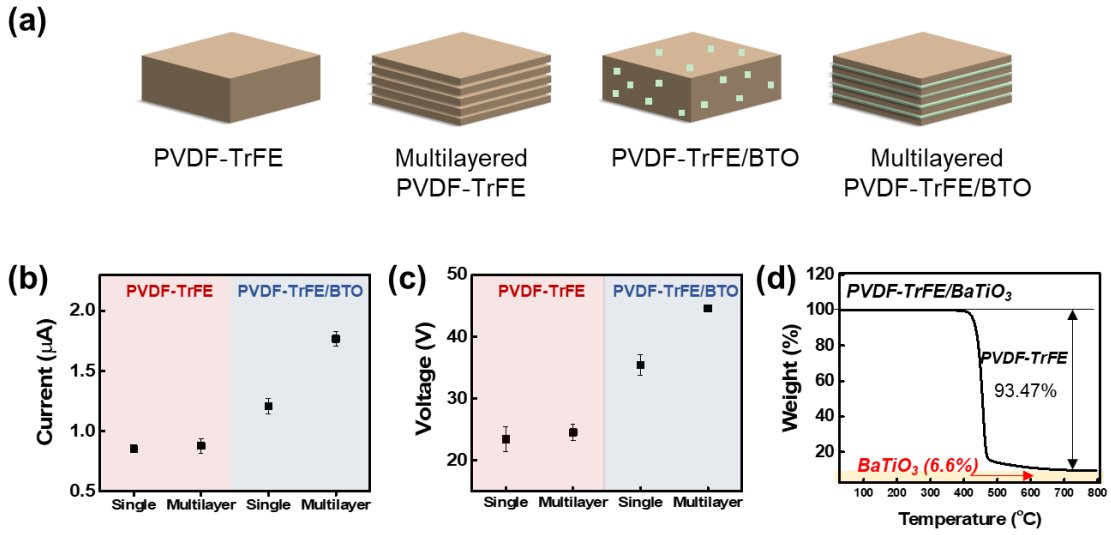

Figure 3.10. (a) Schematics of the four different types of samples with the same thickness: single PVDF-TrFE, multilayered PVDF-TrFE, single PVDF-TrFE/BTO, multilayered PVDF-TrFE/BTO. Comparison of (b) the output current and (c) voltage of the four different types of samples (d) Thermo gravimetric analysis (TGA) result of the four-layerd PVDF-TrFE/BTO film.

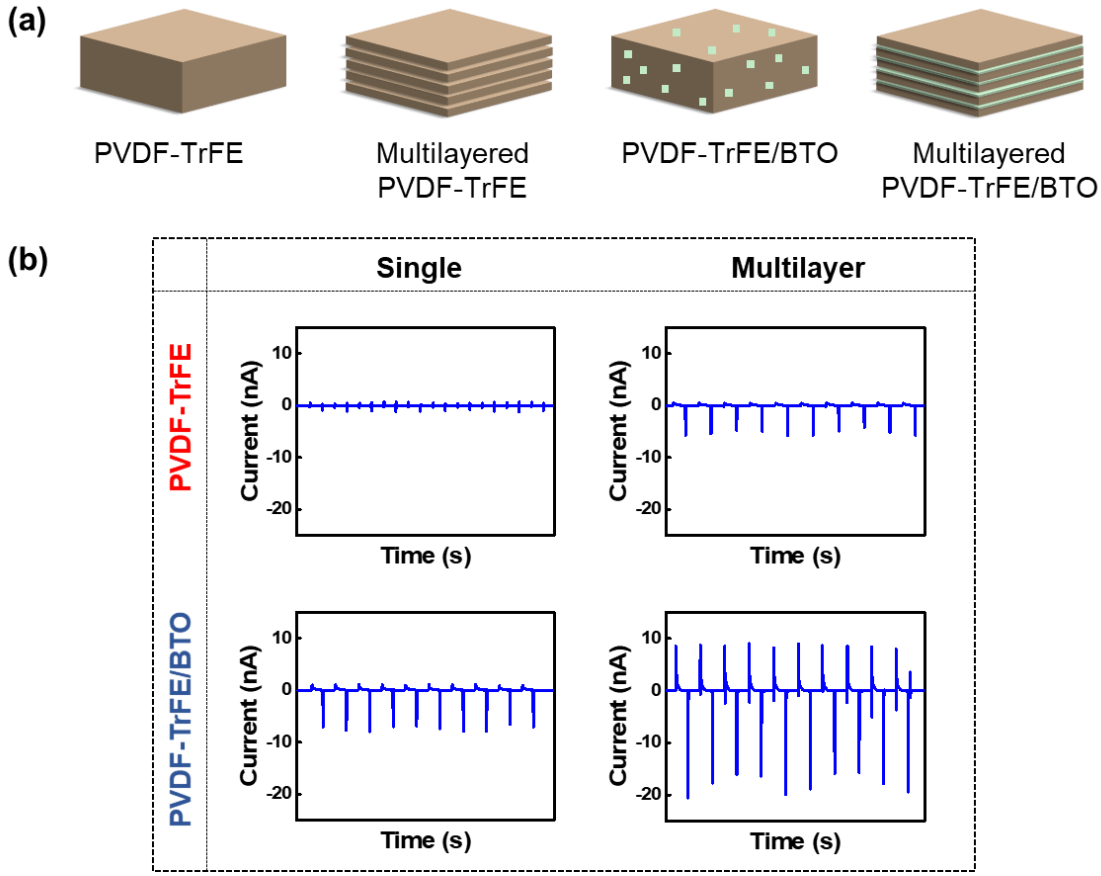

Figure 3.11. (a) Schematics of the four different types of samples with the same thickness: single PVDF-TrFE, multilayered PVDF-TrFE, single PVDF-TrFE/BTO, multilayered PVDF-TrFE/BTO. (b) Piezoelectric current and voltage of the four different types of samples.

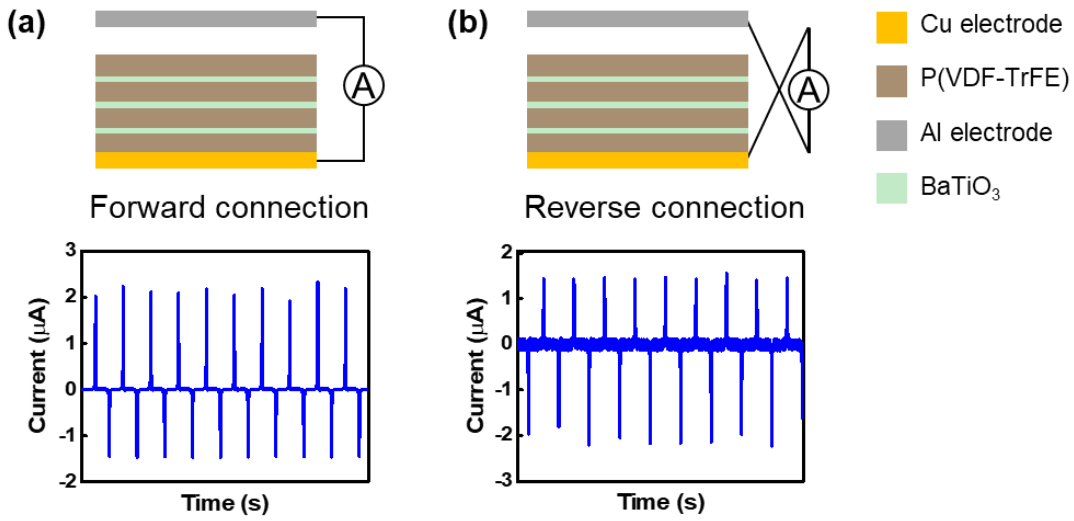

Figure 3.12. Schematics and output current of the TENGs (a) in the forward connection (b) in the reverse connection.

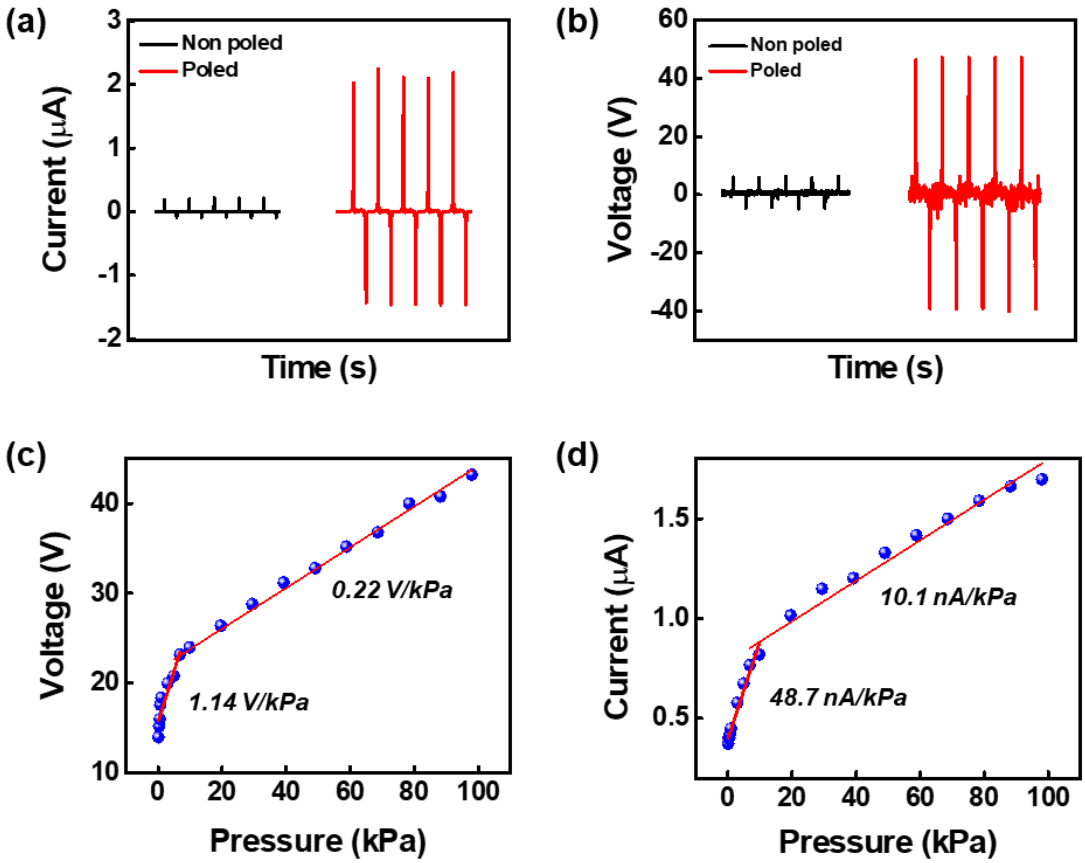

Figure 3.13. (a) Output current and (b) voltage of the non-poled and poled four-layered PVDF-TrFE/BTO film. (c) Output voltage and (d) current of the TENGs depending on the applied pushing force up to 98 kPa.

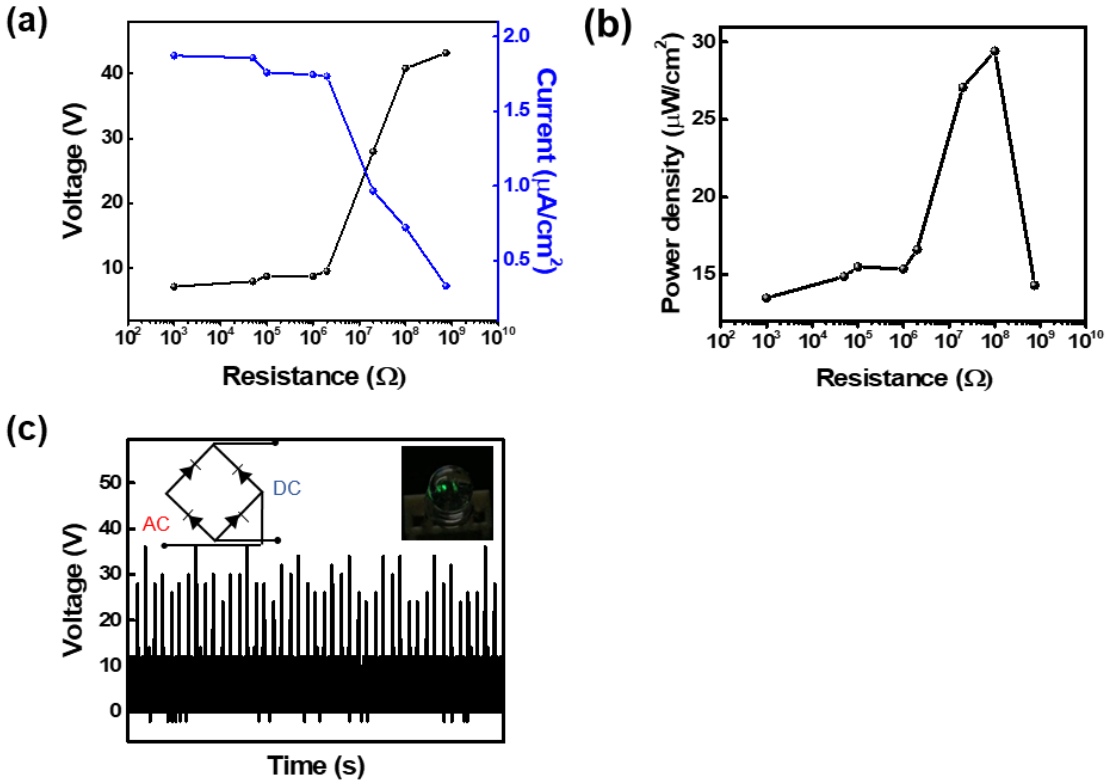

Figure 3.14. (a) Output voltage and current at different loading resistance, ranging from 1 kΩ to 750 MΩ. (b) Optimized maximum output power density at 100 MΩ. (c) Rectified voltage of the four-layerd PVDF-TrFE/BTO film and photographs showing the ability of TENGs to drive LEDs.

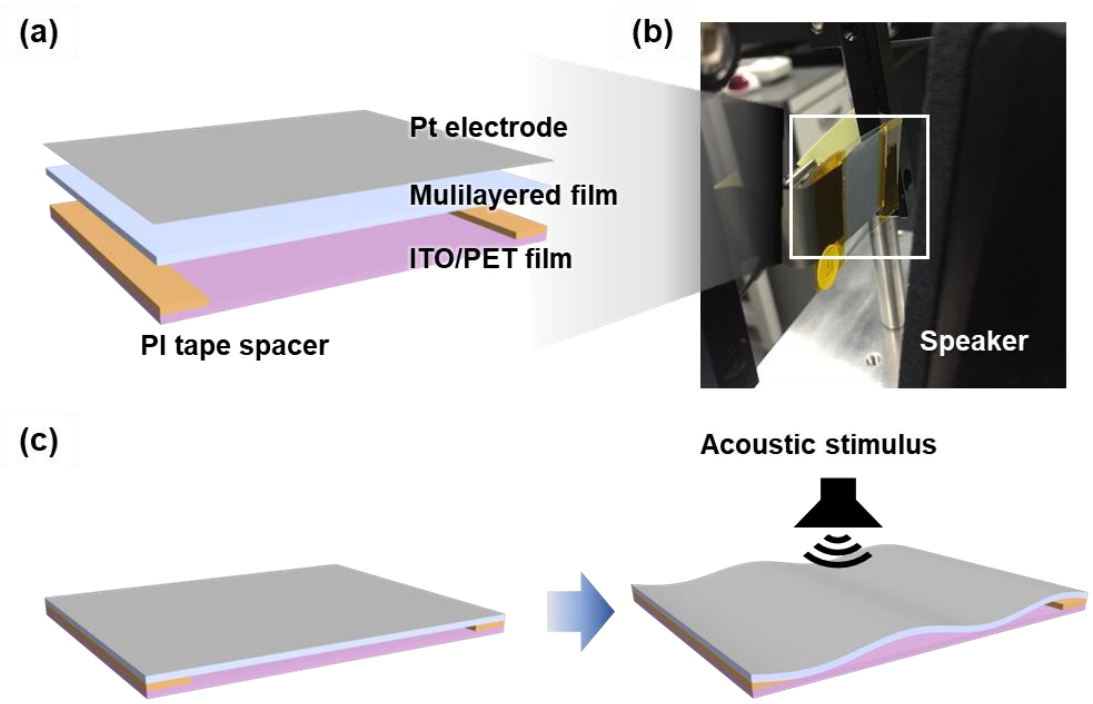

Figure 3.15. (a) Schematic image and (b) photograph of acoustic sensor consists of a multilayered film and ITO/PET film. (c) Schematics of oscillating multilayered film with acoustic energy.

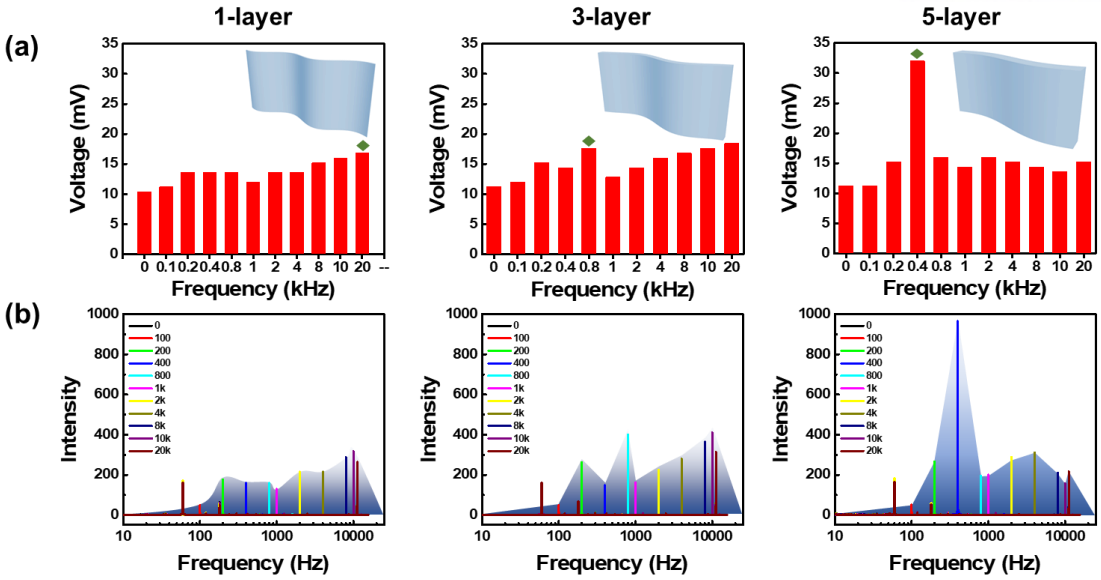

Figure 3.16. Characterization of the frequency selective acoustic sensor. (a) Electrical properties of the acoustic sensor based on multilayered triboelectric nanogenerator. The inset displays the schematics of multilayered film having different oscillating behavior according to the thickness of film. (b) Fast Fourier transform (FFT) of the frequency selective acoustic sensor.

4. Conclusion

In this thesis, we developed the high performance TENGs by the structural design of multilayered PVDF-TrFE and aligned BTO interlayer. The output performance of TENGs is increased by a large surface potential resulting from the high polarization of ferroelectric PVDF-TrFE and high dielectric constant BTO NPs induced by electrical poling process. To further improve the output performance, we fabricated multilayer structures with different numbers of stacking layer. The best output performance can be found at 4-multilayer, which exhibits output current of 1.7 μA and voltage of 43.2 V under applying pressure of 98 kPa. These output values are ~47 % higher output performance compared to single PVDF-TrFE with randomly dispersed BTO NPs. This result is attributed to the more efficient stress transfer to the aligned BTO NPs by multilayered structure. As a further demonstration of high performance TENGs, we applied our TENGs to frequency selective acoustic sensing applications by controlling the thickness of multilayered PVDF-TrFE/BTO film. Our multilayered TENGs provide a great potential in various applications for self-powered sensors and wearable devices.

References

1. Robel, I.; Subramanian, V.; Kuno, M.; Kamat, P. V., Quantum dot solar cells. Harvesting light energy with CdSe nanocrystals molecularly linked to mesoscopic TiO2 films. *Journal of the American Chemical Society* **2006,** *128*, 2385-2393.

2. Raghunathan, V.; Kansal, A.; Hsu, J.; Friedman, J.; Srivastava, M. In *Design considerations for solar energy harvesting wireless embedded systems*, Proceedings of the 4th international symposium on Information processing in sensor networks, IEEE Press: 2005; p 64.

3. Cuadras, A.; Gasulla, M.; Ferrari, V., Thermal energy harvesting through pyroelectricity. *Sensors and Actuators A: Physical* **2010,** *158*, 132-139.

4. Ujihara, M.; Carman, G. P.; Lee, D.-G., Thermal energy harvesting device using ferromagnetic materials. *Applied physics letters* **2007,** *91*, 093508.

5. Li, S.; Yuan, J.; Lipson, H., Ambient wind energy harvesting using cross-flow fluttering. AIP: 2011.

6. Bae, J.; Lee, J.; Kim, S.; Ha, J.; Lee, B.-S.; Park, Y.; Choong, C.; Kim, J.-B.; Wang, Z. L.; Kim, H.-Y., Flutter-driven triboelectrification for harvesting wind energy. *Nature communications* **2014,** *5*, 4929.

7. Xie, Y.; Wang, S.; Lin, L.; Jing, Q.; Lin, Z.-H.; Niu, S.; Wu, Z.; Wang, Z. L., Rotary triboelectric nanogenerator based on a hybridized mechanism for harvesting wind energy. *ACS nano* **2013,** *7*, 7119-7125.

8. Tang, X.; Wang, X.; Cattley, R.; Gu, F.; Ball, A., Energy Harvesting Technologies for Achieving Self-Powered Wireless Sensor Networks in Machine Condition Monitoring: A Review. *Sensors* **2018,** *18*, 4113.

9. Lee, M.; Chen, C. Y.; Wang, S.; Cha, S. N.; Park, Y. J.; Kim, J. M.; Chou, L. J.; Wang, Z. L., A hybrid piezoelectric structure for wearable nanogenerators. *Advanced Materials* **2012,** *24*, 1759-1764.

10. Wen, Z.; Guo, H.; Zi, Y.; Yeh, M.-H.; Wang, X.; Deng, J.; Wang, J.; Li, S.; Hu, C.; Zhu, L., Harvesting broad frequency band blue energy by a triboelectric–electromagnetic hybrid nanogenerator. *ACS nano* **2016,** *10*, 6526-6534.

11. Lin, L.; Xie, Y.; Niu, S.; Wang, S.; Yang, P.-K.; Wang, Z. L., Robust triboelectric nanogenerator based on rolling electrification and electrostatic induction at an instantaneous energy conversion efficiency of～ 55%. *ACS nano* **2015,** *9*, 922-930.

12. Park, K.-I.; Jeong, C. K.; Kim, N. K.; Lee, K. J., Stretchable piezoelectric nanocomposite generator. *Nano Convergence* **2016,** *3*, 12.

13. Yi, F.; Lin, L.; Niu, S.; Yang, P. K.; Wang, Z.; Chen, J.; Zhou, Y.; Zi, Y.; Wang, J.; Liao, Q., Stretchable-rubber-based triboelectric nanogenerator and its application as self-powered body motion sensors. *Advanced Functional Materials* **2015,** *25*, 3688-3696.

14. Wang, Z.; Cheng, L.; Zheng, Y.; Qin, Y.; Wang, Z. L., Enhancing the performance of triboelectric nanogenerator through prior-charge injection and its application on self-powered anticorrosion. *Nano Energy* **2014,** *10*, 37-43.

15. Fan, F.-R.; Lin, L.; Zhu, G.; Wu, W.; Zhang, R.; Wang, Z. L., Transparent triboelectric nanogenerators and self-powered pressure sensors based on micropatterned plastic films. *Nano letters* **2012,** *12*, 3109-3114.

16. Zhou, T.; Zhang, C.; Han, C. B.; Fan, F. R.; Tang, W.; Wang, Z. L., Woven structured triboelectric nanogenerator for wearable devices. *ACS applied materials & interfaces* **2014,** *6*, 14695-14701.

17. Zheng, Q.; Zhang, H.; Shi, B.; Xue, X.; Liu, Z.; Jin, Y.; Ma, Y.; Zou, Y.; Wang, X.; An, Z., In vivo self-powered wireless cardiac monitoring via implantable triboelectric nanogenerator. *Acs Nano* **2016,** *10*, 6510-6518.

18. Niu, S.; Wang, X.; Yi, F.; Zhou, Y. S.; Wang, Z. L., A universal self-charging system driven by random biomechanical energy for sustainable operation of mobile electronics. *Nature communications* **2015,** *6*, 8975.

19. Zhang, L. M.; Han, C. B.; Jiang, T.; Zhou, T.; Li, X. H.; Zhang, C.; Wang, Z. L., Multilayer wavy-structured robust triboelectric nanogenerator for harvesting water wave energy. *Nano Energy* **2016,** *22*, 87-94.

20. Lai, Y. C.; Deng, J.; Zhang, S. L.; Niu, S.; Guo, H.; Wang, Z. L., Single-thread-based wearable and highly stretchable triboelectric nanogenerators and their applications in cloth-based self-powered human-interactive and biomedical sensing. *Advanced Functional Materials* **2017,** *27*, 1604462.

21. Zheng, Q.; Shi, B.; Li, Z.; Wang, Z. L., Recent progress on piezoelectric and triboelectric energy harvesters in biomedical systems. *Advanced Science* **2017,** *4*, 1700029.

22. Fan, F.-R.; Tian, Z.-Q.; Wang, Z. L., Flexible triboelectric generator. *Nano energy* **2012,** *1*, 328-334.

23. Bera, B., Literature review on triboelectric nanogenerator. *Imp J Interdiscip Res* **2016,** *2*, 1263-1271.

24. Song, G.; Kim, Y.; Yu, S.; Kim, M.-O.; Park, S.-H.; Cho, S. M.; Velusamy, D. B.; Cho, S. H.; Kim, K. L.; Kim, J., Molecularly engineered surface triboelectric nanogenerator by self-assembled monolayers (METS). *Chemistry of Materials* **2015,** *27*, 4749-4755.

25. Seung, W.; Yoon, H. J.; Kim, T. Y.; Ryu, H.; Kim, J.; Lee, J. H.; Lee, J. H.; Kim, S.; Park, Y. K.; Park, Y. J., Boosting power-generating performance of triboelectric nanogenerators via artificial control of ferroelectric polarization and dielectric properties. *Advanced Energy Materials* **2017,** *7*, 1600988.

26. Zhu, G.; Pan, C.; Guo, W.; Chen, C.-Y.; Zhou, Y.; Yu, R.; Wang, Z. L., Triboelectric-generator-driven pulse electrodeposition for micropatterning. *Nano letters* **2012,** *12*, 4960-4965.

27. Shin, S.-H.; Bae, Y. E.; Moon, H. K.; Kim, J.; Choi, S.-H.; Kim, Y.; Yoon, H. J.; Lee, M. H.; Nah, J., Formation of triboelectric series via atomic-level surface functionalization for triboelectric energy harvesting. *ACS nano* **2017,** *11*, 6131-6138.

28. Shin, S.-H.; Kwon, Y. H.; Kim, Y.-H.; Jung, J.-Y.; Lee, M. H.; Nah, J., Triboelectric charging sequence induced by surface functionalization as a method to fabricate high performance triboelectric generators. *ACS nano* **2015,** *9*, 4621-4627.

29. Jeong, C. K.; Baek, K. M.; Niu, S.; Nam, T. W.; Hur, Y. H.; Park, D. Y.; Hwang, G.-T.; Byun, M.; Wang, Z. L.; Jung, Y. S., Topographically-designed triboelectric nanogenerator via block copolymer self-assembly. *Nano letters* **2014,** *14*, 7031-7038.

30. Chun, J.; Ye, B. U.; Lee, J. W.; Choi, D.; Kang, C.-Y.; Kim, S.-W.; Wang, Z. L.; Baik, J. M., Boosted output performance of triboelectric nanogenerator via electric double layer effect. *Nature communications* **2016,** *7*, 12985.

31. Yang, W.; Chen, J.; Jing, Q.; Yang, J.; Wen, X.; Su, Y.; Zhu, G.; Bai, P.; Wang, Z. L., 3D stack integrated triboelectric nanogenerator for harvesting vibration energy. *Advanced Functional Materials* **2014,** *24*, 4090-4096.

32. Yang, W.; Chen, J.; Zhu, G.; Yang, J.; Bai, P.; Su, Y.; Jing, Q.; Cao, X.; Wang, Z. L., Harvesting energy from the natural vibration of human walking. *ACS nano* **2013,** *7*, 11317-11324.

33. Xiao, T. X.; Liang, X.; Jiang, T.; Xu, L.; Shao, J. J.; Nie, J. H.; Bai, Y.; Zhong, W.; Wang, Z. L., Spherical Triboelectric Nanogenerators Based on Spring-Assisted Multilayered Structure for Efficient Water Wave Energy Harvesting. *Advanced Functional Materials* **2018,** *28*, 1802634.

34. Cao, X.; Zhang, M.; Huang, J.; Jiang, T.; Zou, J.; Wang, N.; Wang, Z. L., Inductor-Free Wireless Energy Delivery via Maxwell's Displacement Current from an Electrodeless Triboelectric Nanogenerator. *Advanced Materials* **2018,** *30*, 1704077.

35. Zhang, C.; Zhou, T.; Tang, W.; Han, C.; Zhang, L.; Wang, Z. L., Rotating-disk-based direct-current triboelectric nanogenerator. *Advanced Energy Materials* **2014,** *4*, 1301798.

36. Jiang, T.; Chen, X.; Yang, K.; Han, C.; Tang, W.; Wang, Z. L., Theoretical study

on rotary-sliding disk triboelectric nanogenerators in contact and non-contact modes. *Nano Research* **2016,** *9*, 1057-1070.

37. Pu, X.; Li, L.; Song, H.; Du, C.; Zhao, Z.; Jiang, C.; Cao, G.; Hu, W.; Wang, Z. L., A self-charging power unit by integration of a textile triboelectric nanogenerator and a flexible lithium-ion battery for wearable electronics. *Advanced Materials* **2015,** *27*, 2472-2478.

38. Liu, M.; Pu, X.; Jiang, C.; Liu, T.; Huang, X.; Chen, L.; Du, C.; Sun, J.; Hu, W.; Wang, Z. L., Large-Area All-Textile Pressure Sensors for Monitoring Human Motion and Physiological Signals. *Advanced Materials* **2017,** *29*, 1703700.

39. Chen, J.; Huang, Y.; Zhang, N.; Zou, H.; Liu, R.; Tao, C.; Fan, X.; Wang, Z. L., Micro-cable structured textile for simultaneously harvesting solar and mechanical energy. *Nature Energy* **2016,** *1*, 16138.

40. Seung, W.; Gupta, M. K.; Lee, K. Y.; Shin, K.-S.; Lee, J.-H.; Kim, T. Y.; Kim, S.; Lin, J.; Kim, J. H.; Kim, S.-W., Nanopatterned textile-based wearable triboelectric nanogenerator. *ACS nano* **2015,** *9*, 3501-3509.

41. Pu, X.; Li, L.; Liu, M.; Jiang, C.; Du, C.; Zhao, Z.; Hu, W.; Wang, Z. L., Wearable self-charging power textile based on flexible yarn supercapacitors and fabric nanogenerators. *Advanced Materials* **2016,** *28*, 98-105.

42. Zhu, G.; Bai, P.; Chen, J.; Wang, Z. L., Power-generating shoe insole based on triboelectric nanogenerators for self-powered consumer electronics. *Nano Energy* **2013,** *2*, 688-692.

43. Guo, H.; Yeh, M.-H.; Zi, Y.; Wen, Z.; Chen, J.; Liu, G.; Hu, C.; Wang, Z. L., Ultralight cut-paper-based self-charging power unit for self-powered portable electronic and medical systems. *ACS nano* **2017,** *11*, 4475-4482.

44. Lin, L.; Wang, S.; Xie, Y.; Jing, Q.; Niu, S.; Hu, Y.; Wang, Z. L., Segmentally structured disk triboelectric nanogenerator for harvesting rotational mechanical energy. *Nano letters* **2013,** *13*, 2916-2923.

45. Wang, P.; Pan, L.; Wang, J.; Xu, M.; Dai, G.; Zou, H.; Dong, K.; Wang, Z. L., An Ultra-Low-Friction Triboelectric–Electromagnetic Hybrid Nanogenerator for Rotation Energy Harvesting and Self-Powered Wind Speed Sensor. *ACS nano* **2018,** *12*, 9433-9440.

46. Cao, R.; Pu, X.; Du, X.; Yang, W.; Wang, J.; Guo, H.; Zhao, S.; Yuan, Z.; Zhang, C.; Li, C., Screen-printed washable electronic textiles as self-powered touch/gesture tribo-sensors for intelligent human–machine interaction. *ACS nano* **2018,** *12*, 5190-5196.

47. Bai, P.; Zhu, G.; Zhou, Y. S.; Wang, S.; Ma, J.; Zhang, G.; Wang, Z. L., Dipole-moment-induced effect on contact electrification for triboelectric nanogenerators. *Nano Research* **2014,** *7*, 990-997.

48. Lee, K. Y.; Kim, S. K.; Lee, J. H.; Seol, D.; Gupta, M. K.; Kim, Y.; Kim, S. W., Controllable charge transfer by ferroelectric polarization mediated triboelectricity. *Advanced Functional Materials* **2016,** *26*, 3067-3073.

49. Yang, L.; Li, X.; Allahyarov, E.; Taylor, P. L.; Zhang, Q.; Zhu, L., Novel polymer ferroelectric behavior via crystal isomorphism and the nanoconfinement effect. *Polymer* **2013,** *54*, 1709-1728.

50. Hu, W. J.; Juo, D.-M.; You, L.; Wang, J.; Chen, Y.-C.; Chu, Y.-H.; Wu, T., Universal ferroelectric switching dynamics of vinylidene fluoride-trifluoroethylene copolymer films. *Scientific reports* **2014,** *4*, 4772.

51. Kim, M.; Park, D.; Alam, M. M.; Lee, S.; Park, P.; Nah, J., Output Power Density Enhancement of Triboelectric Nanogenerators via Polarized Ferroelectric Polymers and Bulk MoS2 Composites. *ACS nano* **2019**.

52. Lee, J. H.; Hinchet, R.; Kim, T. Y.; Ryu, H.; Seung, W.; Yoon, H. J.; Kim, S. W., Control of skin potential by triboelectrification with ferroelectric polymers. *Advanced materials* **2015,** *27*, 5553-5558.

53. Suo, G.; Yu, Y.; Zhang, Z.; Wang, S.; Zhao, P.; Li, J.; Wang, X., Piezoelectric and triboelectric dual effects in mechanical-energy harvesting using BaTiO3/polydimethylsiloxane composite film. *ACS applied materials & interfaces* **2016,** *8*, 34335-34341.

54. Kwon, Y. H.; Shin, S.-H.; Kim, Y.-H.; Jung, J.-Y.; Lee, M. H.; Nah, J., Triboelectric contact surface charge modulation and piezoelectric charge inducement using polarized composite thin film for performance enhancement of triboelectric generators. *Nano Energy* **2016,** *25*, 225-231.

55. Park, K. I.; Son, J. H.; Hwang, G. T.; Jeong, C. K.; Ryu, J.; Koo, M.; Choi, I.; Lee, S. H.; Byun, M.; Wang, Z. L., Highly-efficient, flexible piezoelectric PZT thin film nanogenerator on plastic substrates. *Advanced materials* **2014,** *26*, 2514-2520.

56. Ha, M.; Lim, S.; Park, J.; Um, D. S.; Lee, Y.; Ko, H., Bioinspired interlocked and hierarchical design of ZnO nanowire arrays for static and dynamic pressure-sensitive electronic skins. *Advanced Functional Materials* **2015,** *25*, 2841-2849.

57. Lai, M.; Cheng, L.; Xi, Y.; Wu, Y.; Hu, C.; Guo, H.; Du, B.; Liu, G.; Liu, Q.; Liu, R., Enhancing the performance of NaNbO3 triboelectric nanogenerators by dielectric modulation and electronegative modification. *Journal of Physics D: Applied Physics* **2017,** *51*, 015303.

58. Hwang, G. T.; Park, H.; Lee, J. H.; Oh, S.; Park, K. I.; Byun, M.; Park, H.; Ahn, G.; Jeong, C. K.; No, K., Self-powered cardiac pacemaker enabled by flexible single

crystalline PMN-PT piezoelectric energy harvester. *Advanced materials* **2014,** *26*, 4880-4887.

59. Shin, S.-H.; Kim, Y.-H.; Lee, M. H.; Jung, J.-Y.; Nah, J., Hemispherically aggregated BaTiO3 nanoparticle composite thin film for high-performance flexible piezoelectric nanogenerator. *Acs Nano* **2014,** *8*, 2766-2773.

60. Gao, T.; Liao, J.; Wang, J.; Qiu, Y.; Yang, Q.; Zhang, M.; Zhao, Y.; Qin, L.; Xue, H.; Xiong, Z., Highly oriented BaTiO 3 film self-assembled using an interfacial strategy and its application as a flexible piezoelectric generator for wind energy harvesting. *Journal of Materials Chemistry A* **2015,** *3*, 9965-9971.

61. Wang, J.; Wu, C.; Dai, Y.; Zhao, Z.; Wang, A.; Zhang, T.; Wang, Z. L., Achieving ultrahigh triboelectric charge density for efficient energy harvesting. *Nature communications* **2017,** *8*, 88.

62. Ali, D.; Yu, B.; Duan, X.; Yu, H.; Zhu, M., Enhancement of output performance through post-poling technique on BaTiO3/PDMS-based triboelectric nanogenerator. *Nanotechnology* **2017,** *28*, 075203.

63. Park, D.; Shin, S.-H.; Yoon, I.-J.; Nah, J., Ferroelectric nanoparticle-embedded sponge structure triboelectric generators. *Nanotechnology* **2018,** *29*, 185402.

64. Pu, X.; Liu, M.; Chen, X.; Sun, J.; Du, C.; Zhang, Y.; Zhai, J.; Hu, W.; Wang, Z. L., Ultrastretchable, transparent triboelectric nanogenerator as electronic skin for biomechanical energy harvesting and tactile sensing. *Science advances* **2017,** *3*, e1700015.

65. Su, L.; Li, H. Y.; Wang, Y.; Kuang, S. Y.; Wang, Z. L.; Zhu, G., Coupling of photoelectric and triboelectric effects as an effective approach for PZT-based high-performance self-powered ultraviolet photodetector. *Nano Energy* **2017,** *31*, 264-269.

66. Park, H.-W.; Huynh, N.; Kim, W.; Hwang, H.; Hong, H.; Choi, K.; Song, A.; Chung, K.-B.; Choi, D., Effects of Embedded TiO2− x Nanoparticles on Triboelectric Nanogenerator Performance. *Micromachines* **2018,** *9*, 407.

67. Yaqoob, U.; Uddin, A. I.; Chung, G.-S., Synthesis of poly (vinylidenefluoride-trifluoroethylene)-0.65 Pb (Mg1/3Nb2/3) O3-0.35 PbTiO3-reduced graphene oxide-composite sheet and its application to flexible energy harvesting. *Composites Part B: Engineering* **2018,** *136*, 92-100.

68. Li, J.; Inukai, K.; Takahashi, Y.; Tsuruta, A.; Shin, W., Thin Film Coating with Highly Dispersible Barium Titanate-Polyvinylpyrrolidone Nanoparticles. *Materials* **2018,** *11*, 712.

69. Mayeen, A.; Kala, M.; Jayalakshmy, M.; Thomas, S.; Rouxel, D.; Philip, J.; Bhowmik, R.; Kalarikkal, N., Dopamine functionalization of BaTiO 3: an effective strategy for the enhancement of electrical, magnetoelectric and thermal properties of BaTiO 3-PVDF-TrFE nanocomposites. *Dalton Transactions* **2018,** *47*, 2039-2051.

70. Sharma, M.; Quamara, J. K.; Gaur, A., Behaviour of multiphase PVDF in (1− x) PVDF/(x) BaTiO 3 nanocomposite films: structural, optical, dielectric and ferroelectric properties. *Journal of Materials Science: Materials in Electronics* **2018,** *29*, 10875-10884.

71. Gao, X.; Zheng, M.; Yan, X.; Fu, J.; Zhu, M.; Hou, Y., The alignment of BCZT particles in PDMS boosts the sensitivity and cycling reliability of a flexible piezoelectric touch sensor. *Journal of Materials Chemistry C* **2019,** *7*, 961-967.

72. Yan, J.; Jeong, Y. G., High performance flexible piezoelectric nanogenerators based on BaTiO3 nanofibers in different alignment modes. *ACS applied materials & interfaces* **2016,** *8*, 15700-15709.

73. Kim, H.; Lee, D.; Kim, D.; Kong, D.; Choi, J.; Lee, M.; Murillo, G.; Jung, J., Dominant Role of Young's Modulus for Electric Power Generation in PVDF–BaTiO3 Composite-Based Piezoelectric Nanogenerator. *Nanomaterials* **2018,** *8*, 777.